actuators

MDPI

Article

An Innovative Three-Dimensional Mathematical–Physical Model for Describing Load-Carrying Characteristic of Hydraulic Supports

Xiang Yuan *, Boyi Yu, Jinghao Zhu, Xinhao Zhou and Yifan Xie

School of Mechanical Engineering, Taiyuan University of Science and Technology, No. 66 Road Waliu, Taiyuan 030024, China; yuboyi2025@126.com (B.Y.); zhujinghao2025@126.com (J.Z.); zhouqinhao2025@126.com (X.Z.); xieyifan2024@126.com (Y.X.)
* Correspondence: yuanxiang@tyust.edu.cn

Abstract

Reliable posture and loading characteristics detection of hydraulic supports is one of the indispensable factors to realizing the intelligentization of fully mechanized coal mining faces. Due to the complexity and dynamic nature of mining process, achieving real-time and accurate detection of the hydraulic support posture and load presents an exceptionally challenging task. Therefore, an interactive algorithm for evaluating the load-carrying characteristic of hydraulic support by considering the three-dimensional space driving theory and dynamic theory was developed and experimentally verified based on a self-designed experimental platform. The paper aimed to establish a three-dimensional spatial dynamic and kinematics model for shield support, evaluating its loading performance in challenging working conditions. Initially, a three-dimensional kinematics model was developed to describe the bearing capacity of powered support in various postures based on the three-dimensional drive space theory. A dynamic model was suggested to investigate the effects of multiple factors on the position of hydraulic support drive units on their load-carrying capability in various demanding working situations. The results indicate that increasing the length of the drive units can significantly improve the bearing performance of shield support. The proposed mathematical technique offers a novel method for modifying the coupling of surrounding rock with hydraulic supports and supplying coal mining with real-time assistance.

Keywords: hydraulic support; bearing performance; three-dimensional kinematics model; fully mechanized coal mining face; coal mining

Check for updates

Academic Editors: Young-Bok Kim and Thinh Huynh

Received: 24 November 2025
Revised: 12 January 2026
Accepted: 12 January 2026
Published: 15 January 2026

Copyright: © 2026 by the authors. Licensee MDPI, Basel, Switzerland. This article is an open access article distributed under the terms and conditions of the Creative Commons Attribution (CC BY) license.

1. Introduction

The fields of aviation, industry, agriculture, and coal mining have made significant contribution of intelligent and unmanned vehicles due to the remarkable improvements of the key technologies [1–4]. The timely and accurate perception of the powered supports provides a continuous supply of support, ensuring a secure mining space for miners and shear, which is an inevitable trend for the construction of the smart mining operations. Considering the complexity and dynamic nature of underground mining activities, the posture and loading detection of the hydraulic support are of utmost importance to stabilize the coal mining space for ensuring the stability of the working scenarios. The ideal functioning performance of hydraulic support in coal mining is hindered by floor and roof tilt, roof breaking, and periodic mining pressure, which have a substantial effect on the

pose characteristics of hydraulic support and alter the performance of the support load in challenging operating environments. Manually adjusting the posture of hydraulic supports poses a risk to the safety of practitioners and reduces the productivity of the mining process. Therefore, an integrated approach for hydraulic support position and load performance must be explored in order to offer effective data monitoring for intelligent coal mining.

Normally, there are two key approaches used to investigate the rock coupling mechanism of hydraulic supports: the posture measurement and the loading characteristic evaluation. The research on the posture measurement mainly focuses on evaluating the pose state of hydraulic supports by obtaining data through sensors, such as establishing a kinematic model of the hydraulic support, reconstructing the model using laser radar or binocular cameras, etc. Such methods can achieve an accuracy of over 90%. As a decisive factor in the intelligentization of the fully mechanized coal mining face, real-time posture detection of powered supports is imperative in ensuring safety and continuous mining, involving AI-driven control [5–11], real-time monitoring [12], and digital twin implementations [13].

With the advancement of artificial intelligence, deep learning has gained remarkable success in a variety of applications, especially its adaptive learning ability in computer vision recognition, such as roads [14,15], medicine [16], agriculture [17], forest fire prevention [18], earthquake early warning [19], and more.

Numerous investigations have been conducted on real-time monitoring and digital twin. A novel Cyber–Physical System-Manufacturing Execution System-Digital Twin Monitoring and Simulation Integrated Platform architecture was proposed to investigate the expected advantages of Digital Twin to perform Digital Twin-Reconfigurable Manufacturing System [20]. In order to improve the real-time and accuracy of fault diagnosis, Zhang et al. performed an intelligent fault diagnosis framework of multi-way directional valve by using deep learning and digital twin [21]. Chen et al. demonstrated the advantages of developing a binocular vision technology that conducted a software development platform and a visual measurement system to predict the posture of advanced hydraulic support [22]. Liang et al. developed a hybrid system that combined Fiber Bragg Grating and Back Propagation neural networks to estimate the real-time and accuracy of support's posture [23]. Hao et al. developed a method for measuring the pose information of shield support by using light detection and range (LidAR) based on digital twin approach and the reconstruction accuracy of over 85% has been experimentally validated [24]. A practical application of a digital twin system was suggested to deal with the difficulties in monitoring the posture and intelligent decision of hydraulic support groups [25]. Chen et al. presented a native approach for acquiring the group pose reconstruction of shield support based on point cloud data, employing the working principles of LiDAR [26]. Li et al. employed a bidirectional digital twin derivation algorithm to evaluate sensing data and identify the pivotal places of the floating connection mechanism [27]. Witek used laboratory testing and numerical computations to investigate the performance of the double-column support foundation [28]. Wan et al. introduced an equilibrium jack structure to mitigate the issue of easy damage to equilibrium jacks [29]. Han addressed the tilt issues associated with hydraulic support at high angles by putting out a four-column shield support strategy that combined support with a moving ram [30]. Furthermore, Ren et al. carried out an experimental comparison to investigate the shield support response using ADAMS simulation as a foundation [31]. Yang established an automated LiDAR-based measurement present for the powered support's attitude concerning the detection robot [32]. Liang developed a fiber sensor to detect the tilting angle of support [33]. Moreover, numerous studies have been carried out on state monitoring of hydraulic support, thereby resulting in significant advancements [32,34–42].

The hypothesis of the loading characteristic evaluation is that the stress and strain of hydraulic supports is obtained by employing the finite element simulation software. Although the finite element analysis method has a relatively reasonable and reliable approach, it has significant limitations in industrial scenarios, which cannot perform online monitoring of the loading characteristics of hydraulic supports. For instance, Peng et al. carried out experiments and finite simulations to determine the operational conditions of hydraulic support [43]. Peng et al. established an experimental loading device and suggested a parallel shield support mechanism [44]. Guo enhanced the safety of the stope by modifying the load estimation method (LOEM) based on the overlaying rock structure of the stope [45]. Kang studied the geomechanical properties of coal, the fundamentals of ground control, and mining techniques for longwall working faces and deep roads [46]. Meng et al. investigated the destruction mechanism of shield support and established an effective approach for analyzing the supporting area under different working conditions [47]. Zhang et al. used ABAQUS to investigate the shield support's response to top coal caving and backfill, with a particular emphasis on the behavior of the support structure to increase the shield support's processing cycle speed [48]. Meng et al. included a multi-software co-simulation approach into by means of electro-mechanical hydraulic coordination simulation to precisely monitor the tilting features of the shield support, allowing for exact monitoring in the analysis [49]. Guan et al. employed a motion-vector closed-loop modeling methodology to illustrate that alterations in the behaviors and the natural frequencies of columns and equilibrium jacks exert an influence on the safety of support utilization [50]. In the context of ultra-high mining hydraulic supports with rigid-flexible coupling characteristics, the proposed model integrates the influence of stiffness variation to improve the precision of the analysis [51].

Previous studies provide insights into investigating the failure processes of hydraulic supports, along with recommendations for preventative actions and particular techniques for solving problems [36,45,52–61]. Notable progress has been made in mitigating the probability of hydraulic support malfunctions, shortening the response time to these incidents, and providing scientific guidance for operational adjustments [30,62,63]. Nevertheless, a significant void remains in the realm of providing direct operational guidelines for the independent positioning and posture adjustment of the supports.

Achieving intelligent production requires improving the intelligence of individual devices, where self-awareness, decision-making ability, self-control, and interconnection across device groups are critical for establishing a positive coal mining agreement. However, operating in enclosed, constrained environments is a challenge for completely mechanized mining. The compact organization of numerical hydraulic support groups and the paucity of information interchange pose additional obstacles to the advancement and implementation of intelligent equipment for these support groups.

The hydraulic support comprises several essential components, including the canopy, front rod, rear rod, columns, equilibrium jack, shield, and base, as illustrated in Figure 1. The columns and the equilibrium jack, as the driving elements of the hydraulic support, play a crucial role in enabling the support to change into a diverse range of postures throughout the working operation. The canopy, which corresponds to the immediate roof, and the base, which is connected to the baseplate, predominantly engage in interactions with the surrounding rock. In coal mining operation, the posture of the canopy provides vital information regarding the attitude of inclination and support height.

Previous studies have mainly focused on the accuracy of pose monitoring for hydraulic supports or the load characteristics of hydraulic supports, with few research results analyzing the coupled load states of hydraulic supports in different pose states, especially in the three-dimensional state of pose and load coupling characteristics. Compared with

previous research results, this paper has achieved real-time load characteristic analysis under different pose states.

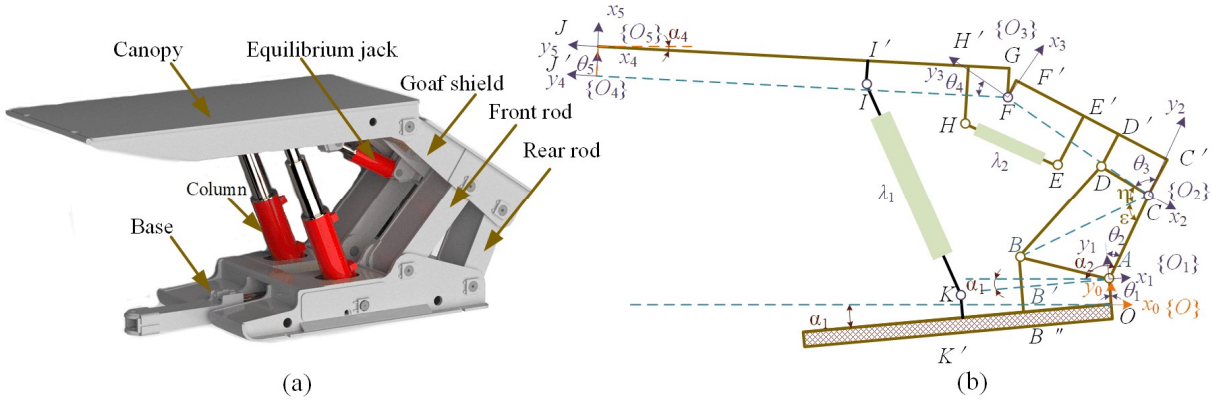


Figure 1. Schematic diagram of the shield support: (**a**) Physical structure of hydraulic support. (**b**) Structural diagram of hydraulic support.

Consequently, a kinematics mathematical algorithm of the shield support is presented by employing Denavit–Hartenberg (D-H) principles in this thesis [60], which simplifies the hydraulic support into a rigid body without considering the elastic deformation that occurs under external loads. Furthermore, a three-dimensional space load-carrying performance model of the powered support based on a two-dimensional kinematic model is developed based on the model mentioned above. Understanding the operating pressure of the drive units plays a crucial role in appropriately foreseeing the response characteristics of the powered support. The three-dimensional structure of a typical powered support is displayed in Figure 2, which offers a visual depiction of the ideas that were addressed. Figure 2a schematically illustrates the mechanical structure diagram of the shield support in three-dimensional space. Figure 2b highlights the canopy in the load-carrying schematic diagram. This study categorizes the relevant information into four distinct spaces: posture space, driving space, joint space, and detection space. Each of these spaces facilitates the mutual exchange of information using different data, thereby enabling the estimation of the tilting angle. The powered support's orientation is governed by the rotation angles of joints θ_1, θ_2, θ_3, θ_4, θ_5, with counter-clockwise defined as the positive direction (Figure 1). The Denavit–Hartenberg (D-H) convention is employed to model the system, using four parameters—link length, joint offset, joint angle, and link twist—to describe each link. Table 1 presents these fundamental D-H parameters.

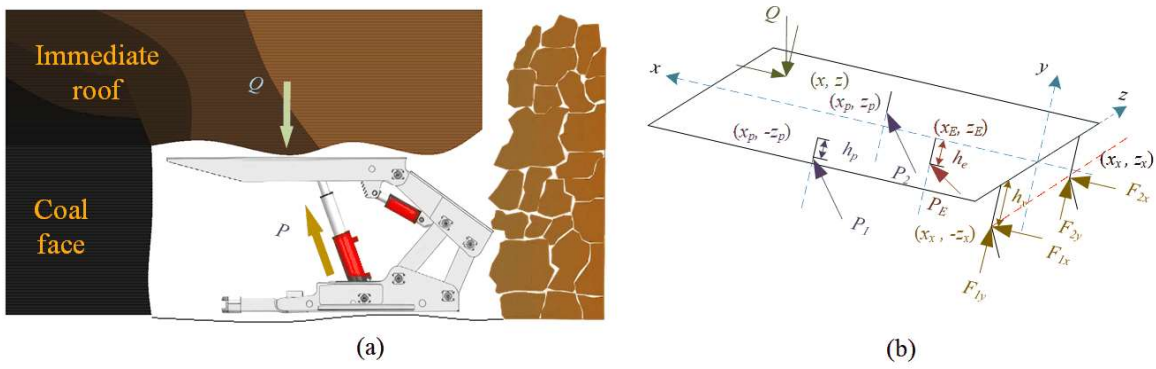


Figure 2. Schematic diagram of the powered support under asymmetric loading conditions: (**a**) Mechanical structure diagram. (**b**) Load-carrying model of canopy.

Table 1. D-H parameters.

Parameter	Label	Rotation Angle, θ_i	Torsion Angle, ϕ_i	The Distance of Joint, d_i
Auxiliary linkage	L_{FG}	θ_5	0	0
Auxiliary canopy	$L_{FJ'}$	θ_4	0	0
Goaf shield	L_{CF}	θ_3	0	0
Rear linkage	L_{AC}	θ_2	0	0
Base	L_{OA}	θ_1	0	0

2. Kinematic Model Analysis of Powered Support

Prior to the establishment of the pose model for the hydraulic support, it is essential to define the relevant coordinate system of the hydraulic support initially. The symbol $OX_nY_nZ_n$ is used to represent the navigation coordinate system, which is essentially an absolute coordinate system, providing a fixed reference framework. On the other hand, $OX_bY_bZ_b$ stands for the carrier coordinate system that is associated with the hydraulic support and moves along with it. The motion posture is realized as a result of the combined effect of rotations that occur, respectively, along the X, Y, and Z axes. ϕ_i is defined as rotation around the Y-axis, and θ_i is defined as rotation around the Z-axis. In addition, φ_i is defined as rotation around the X-axis. The transition from the navigation coordinate system to the carrier coordinate system requires three single axis rotations, namely Z-axis–Y-axis–X-axis.

As a two-degree-of-freedom multi-link equipment, its actuators mainly consist of columns and balance jacks, with the balance jacks used to adjust the support height and canopy angle. The four-bar linkage mechanism is composed of a base, a front link, a rear link, and a shield beam. The canopy that is in direct contact with the immediate roof is regarded as the load-bearing component. To clarify the differences among the various variables, they are divided into four workspaces according to their different functions: drive space, pose space, joint space, and monitoring space. The drive space includes the balance jacks and columns. The pose space is determined by the angular variations of the canopy, shield beam, and base. Meanwhile, the relative pose angle information between the canopy and shield beam, the shield beam and rear link, and the rear link and base is defined as the joint space. During comprehensive mining, the pose space—composed of the position and orientation angle information of the canopy endpoint in the base coordinate system is of great concern. Depending on the direction of transformation between the joint space and pose space, kinematic problems are classified into inverse kinematic methods and forward kinematic methods. The inverse kinematic problem is defined as the transformation from the pose workspace to the joint workspace, while the forward kinematic problem is defined as the transformation from the joint workspace to the pose workspace.

The final rotation matrix is obtained by rotating the absolute coordinate system in the above order, and the specific expression was given as follows.

$$Rot(z,\theta_i) = \begin{bmatrix} \cos\theta_i & -\sin\theta_i & 0 & 0 \\ \sin\theta_i & \cos\theta_i & 0 & 0 \\ 0 & 0 & 1 & 0 \\ 0 & 0 & 0 & 1 \end{bmatrix} \tag{1}$$

$$Rot(x,\varphi_i) = \begin{bmatrix} 1 & 0 & 0 & 0 \\ 0 & \cos\varphi_i & -\sin\varphi_i & 0 \\ 0 & \sin\varphi_i & \cos\varphi_i & 0 \\ 0 & 0 & 0 & 1 \end{bmatrix} \tag{2}$$

$$Rot(y,\phi_i) = \begin{bmatrix} \cos\phi_i & 0 & \sin\phi_i & 0 \\ 0 & 1 & 0 & 0 \\ -\sin\phi_i & 0 & \cos\phi_i & 0 \\ 0 & 0 & 0 & 1 \end{bmatrix} \tag{3}$$

$$RPY(\theta_i,\phi_i,\varphi_i) = Rot(z,\theta_i)Rot(y,\phi_i)Rot(x,\varphi_i) \tag{4}$$

where $RPY(\theta_i, \phi_i, \varphi_i)$ is defined as a rotation matrix that results from the combination of roll, pitch, and yaw. $Rot(z, \theta_i)$, $Rot(y, \phi_i)$ and $Rot(x, \varphi_i)$ represent the rotation matrices of the Z-axis, Y-axis, and X-axis, respectively. Considering the structural characteristics of the hydraulic support, both ϕ_i and φ_i are set to zero.

$${}^{i-1}D_i = \begin{bmatrix} 1 & 0 & 0 & x \\ 0 & 1 & 0 & y \\ 0 & 0 & 1 & z \\ 0 & 0 & 0 & 1 \end{bmatrix} \tag{5}$$

$${}^{i-1}T_i(\theta_i) = {}^{i-1}D_i RPY(\theta_i,\phi_i,\varphi_i) \tag{6}$$

where x, y, and z represent the displacement in the coordinate axis direction from $\{O_{i-1}\}$ to $\{O_i\}$, which is the displacement matrix, and is the transfer matrix from $\{O_{i-1}\}$ to $\{O_i\}$.

In the proposed model, the absolute coordinate system $\{O\}$ is consistent with Cartesian coordinates. The X, Y, and Z axes are, respectively, related to the horizontal, vertical, and vertical directions of the first two axes. As shown in Figure 1, $\{O_1\}$, $\{O_2\}$, $\{O_3\}$, $\{O_4\}$ and $\{O_5\}$ are reference coordinate systems established on the base, rear link, shield beam, auxiliary canopy, and canopy, respectively, represented by $\{x_1Ay_1\}$, $\{x_2Cy_2\}$, $\{x_3Fy_3\}$, $\{x_4J'y_4\}$ and $\{x_5Jy_5\}$. The transfer matrix of the hydraulic support can be obtained as follows.

$$\begin{aligned} {}^{i-1}T_i &= {}^{i-1}D_i(x,y,z)RPY(\theta_i,\phi_i,\varphi_i) \\ &= \begin{bmatrix} \cos\theta_i & -\cos\alpha_i\sin\theta_i & \sin\alpha_i\sin\theta_i & -L_i\sin\theta_i \\ \sin\theta_i & \cos\alpha_i\cos\theta_i & -\sin\alpha_i\sin\theta_i & L_i\cos\theta_i \\ 0 & 0 & 1 & d_i \\ 0 & 0 & 0 & 1 \end{bmatrix} \end{aligned} \tag{7}$$

where α_i (link torsion angle) is a parameter that describes the relative orientation between adjacent link coordinate systems and α_i is equal to 0.

If point A is the origin of coordinate system $\{O_1\}$, then the transfer matrix from $\{O\}$ to $\{O_1\}$ can be expressed as

$${}^0T_1 = \begin{bmatrix} \cos\theta_1 & -\sin\theta_1 & 0 & -L_{OA}\sin\theta_1 \\ \sin\theta_1 & \cos\theta_1 & 0 & L_{OA}\cos\theta_1 \\ 0 & 0 & 1 & 0 \\ 0 & 0 & 0 & 1 \end{bmatrix} \tag{8}$$

Assuming point C is the origin of the $\{O_2\}$ coordinate system, the transfer matrix from $\{O_1\}$ to $\{O_2\}$ is obtained as

$${}^1T_2 = \begin{bmatrix} \cos\theta_2 & -\sin\theta_2 & 0 & -L_{AC}\sin\theta_2 \\ \sin\theta_2 & \cos\theta_2 & 0 & L_{AC}\cos\theta_2 \\ 0 & 0 & 1 & 0 \\ 0 & 0 & 0 & 1 \end{bmatrix} \tag{9}$$

If point F is the origin of coordinate system $\{O_3\}$, then the transfer matrix from $\{O_2\}$ to $\{O_3\}$ is

$$ {}^{2}T_{3} = \begin{bmatrix} \cos\theta_3 & -\sin\theta_3 & 0 & -L_{CF}\sin\theta_3 \\ \sin\theta_3 & \cos\theta_3 & 0 & L_{CF}\cos\theta_3 \\ 0 & 0 & 1 & 0 \\ 0 & 0 & 0 & 1 \end{bmatrix} \tag{10} $$

If point J′ is the origin of coordinate system $\{O_4\}$, then the transfer matrix from $\{O_3\}$ to $\{O_4\}$ is

$$ {}^{3}T_{4} = \begin{bmatrix} \cos\theta_4 & -\sin\theta_4 & 0 & -L_{FJ'}\sin\theta_4 \\ \sin\theta_4 & \cos\theta_4 & 0 & L_{FJ'}\cos\theta_4 \\ 0 & 0 & 1 & 0 \\ 0 & 0 & 0 & 1 \end{bmatrix} \tag{11} $$

If point J is the origin of coordinate system $\{O_5\}$, then the transfer matrix from $\{O_4\}$ to $\{O_5\}$ is

$$ T_{4}^{5} = \begin{bmatrix} \cos\theta_5 & -\sin\theta_5 & 0 & L_{JJ'}\cos\theta_5 \\ \sin\theta_5 & \cos\theta_5 & 0 & L_{JJ'}\sin\theta_5 \\ 0 & 0 & 1 & 0 \\ 0 & 0 & 0 & 1 \end{bmatrix} \tag{12} $$

Based on the above expression, the final transfer matrix expression is given by

$$ \begin{aligned} {}^{0}T_{5} &= \prod_{i=1}^{5} {}^{i-1}T_{i}(\theta_i) = {}^{0}T_{1}(\theta_1){}^{1}T_{2}(\theta_2){}^{2}T_{3}(\theta_3){}^{3}T_{4}(\theta_4){}^{4}T_{5}(\theta_5) \\ &= \left[\begin{array}{c|c} T & D \\ \hline 0 & 1 \end{array}\right] = \left[\begin{array}{ccc|c} n_x & o_x & a_x & d_x \\ n_y & o_y & a_y & d_y \\ n_z & o_z & a_z & d_z \\ \hline 0 & 0 & 0 & 1 \end{array}\right] \end{aligned} \tag{13} $$

Considering that displacement only depends on the translation of the coordinate origin, the expression for the displacement matrix from point O in the absolute coordinate system $\{O\}$ to point J in the coordinate system $\{O_5\}$ is

$$ \begin{bmatrix} d_x \\ d_y \\ d_z \end{bmatrix} = \begin{bmatrix} L_{JJ'}c_{12345} - L_{FJ'}s_{1234} - L_{CF}s_{123} - L_{AC}s_{12} - L_{OA}s_1 \\ L_{JJ'}s_{12345} + L_{FJ'}c_{1234} + L_{CF}c_{123} + L_{AC}c_{12} + L_{OA}c_1 \\ 0 \end{bmatrix} \tag{14} $$

After the translation and rotation of the coordinate system, the final transformation matrix can be obtained.

$$ {}^{0}T_{5} = \begin{bmatrix} c_{12345} & -s_{12345} & 0 & L_{JJ'}c_{12345} - L_{FJ'}s_{1234} - L_{CF}s_{123} - L_{AC}s_{12} - L_{OA}s_1 \\ s_{12345} & c_{12345} & 0 & L_{JJ'}s_{12345} + L_{FJ'}c_{1234} + L_{CF}c_{123} + L_{AC}c_{12} + L_{OA}c_1 \\ 0 & 0 & 1 & 0 \\ 0 & 0 & 0 & 1 \end{bmatrix} \tag{15} $$

where s represents sin, and c represents cos. 1, 2, 3, 4 and 5 represent the rotation angle information of the joint, which are θ_1, θ_2, θ_3, θ_4 and θ_5, respectively.

From the above equations, the position information of each point in the absolute coordinate system $\{O\}$ can be obtained as follows. The relevant parameter values are shown in Table 2.

$$ P(x^0, y^0, z^0, 1) = \prod_{i=1}^{n} \left\{ {}^{i-1}T_{i}(\theta_i) \right\} P(x^i, y^i, z^i, 1) \quad n = 5 \tag{16} $$

where x, y and z, respectively, represent the corresponding position coordinates in different coordinate systems.

$$P(x^0_{\times\times}, y^0_{\times\times}, z^0_{\times\times}, 1) = \prod_{i=1}^{5}\left\{{}^{i-1}T_i(\theta_i)\right\}P(x^5_{\times\times}, y^5_{\times\times}, z^5_{\times\times}, 1) = \left[\begin{array}{c|c} T & P \\ \hline 0 & 1 \end{array}\right] = \left[\begin{array}{ccc|c} n_x & o_x & a_x & p_x \\ n_y & o_y & a_y & p_y \\ n_z & o_z & a_z & p_z \\ \hline 0 & 0 & 0 & 1 \end{array}\right] \tag{17}$$

where P is the coordinate point of the top beam, and T is the rotation matrix from $\{O\}$ to $\{O_5\}$; $\vec{n}$, $\vec{o}$, $\vec{a}$ represent normal vector, directional vector, and proximity vector, respectively. The number 1 is a proportionality coefficient, representing the transformation coefficient from the homogeneous coordinates of the position vector to the physical coordinates of the transformation vector. It is solved in standard Euclidean space, so the coefficient is equal to 1.

Table 2. Basic parameters.

Base		Goaf Shield		Canopy		Four-Bar Linkage	
Parameters	**Values**	**Parameters**	**Values**	**Parameters**	**Values**	**Parameters**	**Values**
L_{OA}	131	$L_{EE'}$	288	L_{FG}	150	$L_{CC'}$	206
$L_{BB''}$	282	$L_{C'F'}$	873	L_{GJ}	2115	$L_{DD'}$	188
$L_{OB''}$	450	$L_{D'F'}$	588	$L_{HH'}$	300	$L_{C'D'}$	285
$L_{OI'}$	763	$L_{FF'}$	96	$L_{GH'}$	211	L_{AC}	484
$L_{II'}$	114	$L_{C'E'}$	482	$L_{GI'}$	730	L_{BD}	632

3. Analysis of the Supporting Behavior

The proposed mathematical model assumption is based on the following principles:

(1) Assuming that the working pressure of the hydraulic support remains below the working pressure of the safety valve. The reason is that if the pressure goes beyond the pre-set opening pressure of the safety valve, the column or the balance jack will release pressure, causing the working pressure to change.

(2) Given that the working pressure of the safety valve set in the actual production process ensures the safety and reliability of the hydraulic support, it can be assumed that the structural components of the support remain free from elastic deformation under load.

(3) The influence of excessive load due to transient impact on the deformation of the hydraulic support is ignored. The reason is that when the impact time is too short, the column safety valve of the hydraulic support cannot respond rapidly and release pressure promptly, which in turn leads to the deformation of the support.

(4) Within the kinematic model of the hydraulic support, the effect of the clearance among the relevant components of the hydraulic support on the exact pose of the support is intentionally ignored.

Based on the above assumptions, the moment of the straight line O'O" established by joining the front-rear linkage intersection sites with each force is considered, with the goaf shield and canopy acting as entities for isolation. The balanced equation is shown below.

$$r_1[P_1(x,z) + P_2(x,z)] + [H_0 + b_c\tan(\varphi + \alpha_{4,z})]Q(x,z)f_{cs} - (x + b_c)Q(x,z)\cos(-\alpha_{4,z}) = 0 \tag{18}$$

where P_1 and P_2 represent the operating pressure of the columns, respectively. r_1 represents the distance from the instantaneous center of the four-link mechanism to the column. x and z are the positions where external loads act on the top beam in the x and z directions, respectively. H_0 is the distance from the hinge position of the goaf shield to the canopy. Q is the external load acting on the canopy. $\alpha_{4,z}$ is the inclination angle of the canopy. φ

is the angle between the instantaneous center of the four-link mechanism and the hinge position of the goaf shield and canopy, and the X-axis direction. b_c is the distance from the instantaneous center of the four-link mechanism to the canopy. f represents the frictional factor between the canopy and the immediate roof, $f \in (0, 0.3)$. The size of the frictional factor is subject to change and may vary between countries. Different sources suggest values such as 0.1 or 0.3 [60]. In the present study, f is set to 0.3. The force balance equation in the horizontal direction can be obtained $f_{cs} = f\cos(-\alpha_{4,z}) + \sin(-\alpha_{4,z})$.

$$fQ(x,z)\cos(-\alpha_{4,z})\cos(-\alpha_{4,z}) + \left[\begin{array}{l}(F_1(x,z)+F_{1'}(x,z))\sin\alpha_1 + (F_2(x,z)+\\ F_{2'}(x,z))\sin\alpha_2 - (P_1(x,z)+P_2(x,z))\sin\beta\end{array}\right] = 0 \tag{19}$$

where F_1 and $F_{1'}$ denote the force acting on the left and right front linkages, respectively. F_2 and $F_{2'}$ represent the force acting on the left and right rear linkages, respectively. α_1 denotes the inclination of the front linkage relative to the horizontal opposite. α_2 denotes the inclination of the rear linkage relative to the horizontal opposite. β represents the angle of the column in the Y-axis direction. Balancing forces in the vertical direction can be expressed as

$$\left\{\begin{array}{l}[P_1(x,z)+P_2(x,z)]\cos\beta\\ +[F_1(x,z)+F_{1'}(x,z)]\cos\alpha_1\end{array}\right\} + \left\{\begin{array}{l}[F_2(x,z)+F_{2'}(x,z)]\cos\alpha_2 -\\ [Q(x,z)+fQ(x,z)\cos(-\alpha_{4,z})\sin(-\alpha_{4,z})]\end{array}\right\} = 0 \tag{20}$$

As an isolated body, the moment balance equation for each force of the canopy on point O can be expressed as

$$r_2[P_1(x,z)+P_2(x,z)] + tP_E(x,z) + Q(x,z)[H_0 f_{cs} - x\cos(-\alpha_{4,z})] = 0 \tag{21}$$

where P_E denotes the working pressure of the equilibrium jack. r_2 signifies the distance from the junction point of the canopy and the goaf shield to the column. t refers to the distance from the instantaneous center of the four-link mechanism to the balance bar.

Focusing on the canopy as the research object, the equation can be derived.

(1) The moment expression considering the canopy is obtained.

$$\left\{\begin{array}{l}-[fQ(x,z)\cos(-\alpha_{4,z}) + Q(x,z)\sin(-\alpha_{4,z})]+\\ \left[\begin{array}{l}(P_1(x,z)+P_2(x,z))\sin\alpha_{11} + P_E(x,z)\sin\alpha_{22}\\ +[F_{1s}(x,z)+F_{2s}(x,z)]\sin\beta_{11}\end{array}\right]\end{array}\right\} = 0 \tag{22}$$

where α_{11} denotes the angle between the direction perpendicular to the canopy and the column. α_{22} signifies the angle between the equilibrium jack and the direction perpendicular to the canopy. F_{1s} and F_{2s} represent the applied force acting on the shaft of the pin located on the left and left sides, respectively $\beta_{11} = a\tan(F_{1sx}/F_{1sy})$.

(2) The moment expression perpendicular to the canopy can be mathematically expressed as

$$\left\{\begin{array}{l}-Q(x,z)\cos(-\alpha_{4,z})+\\ [P_1(x,z)+P_2(x,z)]\cos\alpha_{11}\end{array}\right\} + \left\{\begin{array}{l}P_E(x,z)\cos\alpha_{22}+\\ [F_1(x,z)+F_2(x,z)]\cos\beta_{11}\end{array}\right\} = 0 \tag{23}$$

(3) As shown in Figure 2b, the moment in the XOY plane is horizontal, so that the moment expression can be expressed as

$$[fQ(x,z)\cos(-\alpha_{4,z}) + Q(x,z)\sin(-\alpha_{4,z})]z + \left\{\begin{array}{l}[P_2(x,z)-P_1(x,z)]\sin\alpha_{11}z_P+\\ [F_1(x,z)-F_2(x,z)]\sin\beta_{11}z_J\end{array}\right\} = 0 \tag{24}$$

where z represents the Z-axis coordinates of different joint points of the hydraulic support. z_P, z_J denote coordinate of the equilibrium in the width direction of canopy and the articulation point between column and canopy in the width direction of canopy, respectively.

(4) The moment concerning the XOY plane in the vertical direction, and the moment equation can be calculated.

$$-Q(x,z)\cos(-\alpha_{4,z})z + \left\{ \begin{array}{l} [P_2(x,z) - P_1(x,z)]\cos\alpha_{11}z_P + \\ [F_2(x,z) - F_1(x,z)]\cos\beta_{11}z_J \end{array} \right\} = 0 \tag{25}$$

(5) Taking the moment on the Z-axis, the torque balance equation can be written as

$$-Q(x,z)\cos(-\alpha_{4,z})x + \left\{ \begin{array}{l} [P_1(x,z) + P_2(x,z)]\cos\alpha_{11}x_P \\ +[P_1(x,z) + P_2(x,z)]\sin\alpha_{11}h_P \\ +P_E(x,z)\sin\alpha_{22}h_T + P_E(x,z)\cos\alpha_{22}x_T \\ +[F_{1s}(x,z) + F_{2s}(x,z)]\sin\beta_{11}h_x \end{array} \right\} = 0 \tag{26}$$

where h_P, represents the distance from the junction point of the column and the canopy to the column. h_T represents the distance from the junction point of the equilibrium jack and the canopy to the column. h_e denotes the distance between the connection of the equilibrium jack on the canopy, and h_x denotes the distance from the hinge point F to the canopy. x_P, x_T refers to the distance from the end of the canopy to the installation point of the column and equilibrium jack. F_{1s}, $F_{2s,}$ respectively, represent the loads acting on the left and right pin shafts, which are the hinge points between the canopy and shield beams.

4. Canopy Loading Characteristic Based on Column Adaptive Model

(1) The carrying characteristic of the canopy in this interval can be mathematically expressed as:

$$\left\{ \begin{array}{l} Q_1_T_1(x,z) = \frac{r_1 t P_L(x,z)}{(r_1-r_2)[x\cos(-\alpha_{4,z}) - H_0 f_{cs}] - b_c r_2[\cos(-\alpha_{4,z}) - \tan(\varphi+\alpha_{4,z})f_{cs}]} \\ Q_1_T_2(x,z) = \frac{r_1 t P_L(x,z)}{(r_1-r_2)[x\cos(-\alpha_{4,z}) - H_0 f_{cs}] - b_c r_2[\cos(-\alpha_{4,z}) - \tan(\varphi+\alpha_{4,z})f_{cs}]} \end{array} \right. \tag{27}$$

where P_L represents the initial support force of the left and right pillars. $Q_1_T_1$ and $Q_1_T_2$ refer to the loads in two different areas on the left and right, respectively.

(2) The carrying characteristic of the canopy in the column working area can be expressed by the following equation:

$$\left\{ \begin{array}{l} Q_2_P_1(x,z) = \frac{2r_1 P_{1\max}(x,z)\sin(\alpha_{11}-\beta_{11})z_P}{[(b_c+x)\cos(-\alpha_{4,z}) - H_b f_{cs}]\sin(\alpha_{11}-\beta_{11})z_P - r_1 f_{cc} z} \\ Q_2_P_2(x,z) = \frac{2r_1 P_{2\max}(x,z)\sin(\alpha_{11}-\beta_{11})z_P}{[(b_c+x)\cos(-\alpha_{4,z}) - H_b f_{cs}]\sin(\alpha_{11}-\beta_{11})z_P + r_1 f_{cc} z} \end{array} \right. \tag{28}$$

where $f_{cc} = f_{cs}\cos\beta_{11} - \cos(-\alpha_{4,z})\sin\beta_{11}$, $H_b = H_0 + b_c\tan(\varphi+\alpha_{4,z})$. $Q_2_P_1$, $Q_2_P_2$ refer to the loads in two different areas on the left and right, respectively. $P_{1\max}$ and $P_{2\max,}$ respectively, represent the maximum operating pressure of the left and right columns.

(3) The expression for the load characteristic of the canopy can be obtained from the following expression.

$$\left\{ \begin{array}{l} Q_3_T_1(x,z) = \frac{r_1 t P_Y(x,z)}{(r_1-r_2)[x\cos(-\alpha_{4,z}) - H_0 f_{cs}] - b_c r_2[\cos(-\alpha_{4,z}) - \tan(\varphi+\alpha_{4,z})f_{cs}]} \\ Q_3_T_2(x,z) = \frac{r_1 t P_Y(x,z)}{(r_1-r_2)[x\cos(-\alpha_{4,z}) - H_0 f_{cs}] - b_c r_2[\cos(-\alpha_{4,z}) - \tan(\varphi+\alpha_{4,z})f_{cs}]} \end{array} \right. \tag{29}$$

where P_Y represents the working resistance of the left and right columns. $Q_3_T_1$ and $Q_3_T_2$ refer to the loads in two different areas on the left and right, respectively. The critical point between the tension zone of the drive units is calculated.

$$\begin{cases} Q_1_T_1(x,z) = Q_2_P_1(x,z) \\ Q_1_T_2(x,z) = Q_2_P_2(x,z) \end{cases} \tag{30}$$

Accordingly, critical points can be obtained from the following expression:

$$\begin{cases} x_1_P_1(x,z) = \frac{tP_L(x,z)\left\{[b_c\cos(-\alpha_{4,z})-H_b f_{cs}]\sin(\alpha_{11}-\beta_{11})z_P - r_1 f_{cc} z\right\}+2P_{1\max}(x,z)\sin(\alpha_{11}-\beta_{11})z_P f_{ss}}{[2P_{1\max}(x,z)(r_1-r_2)-tP_L(x,z)]\cos(-\alpha_{4,z})\sin(\alpha_{11}-\beta_{11})z_P} \\ x_1_P_2(x,z) = \frac{tP_L(x,z)\left\{[b_c\cos(-\alpha_{4,z})-H_b f_{cs}]\sin(\alpha_{11}-\beta_{11})z_P + r_1 f_{cc} z\right\}+2P_{2\max}(x,z)\sin(\alpha_{11}-\beta_{11})z_P f_{ss}}{[2P_{2\max}(x,z)(r_1-r_2)-tP_L(x,z)]\cos(-\alpha_{4,z})\sin(\alpha_{11}-\beta_{11})z_P} \end{cases} \tag{31}$$

where P_L denotes the tensile operating pressure of the equilibrium jack. $x_1_P_1$ and $x_1_P_2$, respectively, represent the boundary points between the tension working area of the equilibrium jack corresponding to the left and right columns and the working area of the columns.

The critical point between the column work area and the balanced jack compression work area can be determined from the following expression.

$$\begin{cases} Q_2_P_1(x,z) = Q_3_T_1(x,z) \\ Q_2_P_2(x,z) = Q_3_T_2(x,z) \end{cases} \tag{32}$$

Similarly, critical point coordinates can be obtained using the following expressions:

$$\begin{cases} x_2_P_1(x,z) = \frac{tP_Y(x,z)\left\{[b_c\cos(-\alpha_{4,z})-H_b f_{cs}]\sin(\alpha_{11}-\beta_{11})z_P - r_1 f_{cc} z\right\}+2P_{1\max}(x,z)\sin(\alpha_{11}-\beta_{11})z_P f_{ss}}{[2P_{1\max}(x,z)(r_1-r_2)-tP_Y(x,z)]\cos(-\alpha_{4,z})\sin(\alpha_{11}-\beta_{11})z_P} \\ x_2_P_2(x,z) = \frac{tP_Y(x,z)\left\{[b_c\cos(-\alpha_{4,z})-H_b f_{cs}]\sin(\alpha_{11}-\beta_{11})z_P + r_1 f_{cc} z\right\}+2P_{2\max}(x,z)\sin(\alpha_{11}-\beta_{11})z_P f_{ss}}{[2P_{2\max}(x,z)(r_1-r_2)-tP_Y(x,z)]\cos(-\alpha_{4,z})\sin(\alpha_{11}-\beta_{11})z_P} \end{cases} \tag{33}$$

where $x_2_P_1$, $x_2_P_2$, respectively, represent the boundary points between the working area of the left and right columns and the compressed working area of the equilibrium jack.

5. Response Characteristics of the Left and Right Pins

(1) The moment expression parallel to the canopy direction can be written as

$$-[fQ(x,z)\cos(-\alpha_{4,z})+Q(x,z)\sin(-\alpha_{4,z})]+\left\{\begin{array}{l}[P_1(x,z)+P_2(x,z)]\sin\alpha_{11}+\\ P_E(x,z)\sin\alpha_{22}+[F_{1Y}(x,z)+F_{2Y}(x,z)]\end{array}\right\}=0 \tag{34}$$

where F_{1Y} and F_{2Y} represent the force on the corresponding pin axis parallel to the canopy direction, respectively.

(2) The moment expression perpendicular to the canopy is given by

$$-Q(x,z)\cos(-\alpha_{4,z})+\left\{\begin{array}{l}[P_1(x,z)+P_2(x,z)]\cos\alpha_{11}+\\ P_E(x,z)\cos\alpha_{22}+[F_{1X}(x,z)+F_{2X}(x,z)]\end{array}\right\}=0 \tag{35}$$

where F_{1X} and F_{2X} represent the force on the corresponding pin axis perpendicular to the canopy, respectively.

(3) Taking the moment in the horizontal direction on the XOY plane, the torque balance equation can be written as

$$[fQ(x,z)\cos(-\alpha_{4,z})+Q(x,z)\sin(-\alpha_{4,z})]z+\left\{\begin{array}{l}[P_2(x,z)-P_1(x,z)]\sin\alpha_{11}z_P\\ +[F_{1X}(x,z)-F_{2X}(x,z)]z_J\end{array}\right\}=0 \tag{36}$$

(4) Taking the moment in the vertical direction on the XOY plane, the moment balance equation can be expressed.

$$-Q(x,z)\cos(-\alpha_{4,z})z+\left\{\begin{array}{l}[P_2(x,z)-P_1(x,z)]\cos\alpha_{11}z_P\\+[F_{2Y}(x,z)-F_{1Y}(x,z)]z_J\end{array}\right\}=0 \tag{37}$$

The mechanical response of the left and right pin shafts in the hydraulic support is as follows:

$$\left\{\begin{array}{l}F_{1Y}(x,z)=\frac{Q(x,z)\cos(-\alpha_{4,z})(z_J-z)-[P_1(x,z)+P_2(x,z)]\cos\alpha_{11}z_J+\left\{\begin{array}{l}[P_2(x,z)-P_1(x,z)]\cos\alpha_{11}z_P\\-P_E(x,z)\cos\alpha_{11}z_J\end{array}\right\}}{2z_J}\\F_{2Y}(x,z)=\frac{Q(x,z)\cos(-\alpha_{4,z})(z_J+z)-[P_1(x,z)+P_2(x,z)]\cos\alpha_{11}z_J-\cos\alpha_{11}z_P-P_E(x,z)\cos\alpha_{11}z_J}{2z_J}\end{array}\right. \tag{38}$$

$$\left\{\begin{array}{l}F_{1X}(x,z)=\frac{Q(x,z)f_{cs}(z_J-z)-[P_1(x,z)+P_2(x,z)]\sin\alpha_{11}z_J+\left\{\begin{array}{l}[P_2(x,z)-P_1(x,z)]\sin\alpha_{11}z_P\\-P_E(x,z)\sin\alpha_{11}z_J\end{array}\right\}}{2z_J}\\F_{2X}(x,z)=\frac{Q(x,z)f_{cs}(z_J+z)-[P_1(x,z)+P_2(x,z)]\sin\alpha_{11}z_J-\left\{\begin{array}{l}[P_2(x,z)-P_1(x,z)]\sin\alpha_{11}z_P\\+P_E(x,z)\sin\alpha_{11}z_J\end{array}\right\}}{2z_J}\end{array}\right. \tag{39}$$

Q represents the external force of the canopy.

6. Response of the Four Connecting Bars of Powered Supports

The mechanical performance of the four-link mechanism of the hydraulic supports in three-dimensional space can be determined by the following expression:

$$\left\{\begin{array}{l}F_1(x,z)+F_1{}'(x,z)=\frac{\left\{\begin{array}{l}Q(x,z)\{\tan\alpha_2+f\cos(-\alpha_{4,z})[\sin(-\alpha_{4,z})\tan\alpha_2+\cos(-\alpha_{4,z})]\}\\-[P_1(x,z)+P_2(x,z)](\sin\beta+\cos\beta\tan\alpha_2)\end{array}\right\}}{\cos\alpha_1\tan\alpha_2-\sin\alpha_1}\\F_2(x,z)+F_2{}'(x,z)=\frac{Q(x,z)+fQ(x,z)\cos(-\alpha_{4,z})\sin(-\alpha_{4,z})-\left\{\begin{array}{l}[P_1(x,z)+P_2(x,z)]\cos\beta\\+F_1(x,z)\cos\alpha_1\end{array}\right\}}{\cos\alpha_2}\end{array}\right. \tag{40}$$

Within the XOY plane, with the goaf shield and the canopy being chosen as the research foci, and after performing the operation of taking the moment in the vertical direction, the moment balance equation can be achieved.

$$\left\{\begin{array}{l}-Q(x,z)\cos(-\alpha_{4,z})z+\\[P_2(x,z)-P_1(x,z)]\cos\alpha_{11}z_P\end{array}\right\}+\left\{\begin{array}{l}[F_2{}'(x,z)-F_2(x,z)]\cos(\alpha_2+\alpha_{4,z})z_x\\+[F_1{}'(x,z)-F_1(x,z)]\cos(\alpha_1+\alpha_{4,z})z_x\end{array}\right\}=0 \tag{41}$$

where α_1 and α_2 denote the tilting attitude of the four-link mechanism relative to the canopy in parallel and vertical directions, respectively. F_1 and $F_1{}'$ denote the front connecting rod force corresponding to P_1 and P_2 intervals, respectively. F_2 and $F_2{}'$ denote the rear connecting rod force corresponding to P_1 and P_2 intervals, respectively.

The canopy and goaf shield are selected as the research objects in the XOY plane, Subsequently, by taking the moment in the horizontal direction. The moment expression is obtained.

$$\left\{\begin{array}{l}F_1{}'(x,z)-F_1(x,z)=\frac{Q(x,z)\cos(-\alpha_{4,z})z-\left\{\begin{array}{l}[P_2(x,z)-P_1(x,z)]\cos\alpha_{11}z_P\\+[F_2{}'(x,z)-F_2(x,z)]\cos(\alpha_2+\alpha_{4,z})z_x\end{array}\right\}}{\cos(\alpha_1+\alpha_{4,z})z_x}\\F_2{}'(x,z)-F_2(x,z)=\frac{Q(x,z)\cos(-\alpha_{4,z})z-\left\{\begin{array}{l}[P_2(x,z)-P_1(x,z)]\cos\alpha_{11}z_P\\+[F_1{}'(x,z)-F_1(x,z)]\cos(\alpha_1+\alpha_{4,z})z_x\end{array}\right\}}{\cos(\alpha_2+\alpha_{4,z})z_x}\end{array}\right. \tag{42}$$

Based on Equations (41) and (42), the loading characteristic of the front connecting rod corresponding to the right pillar can be formulated as

$$F_1'(x,z) = \frac{Q(x,z)\left\{\tan\alpha_2 + f\cos(-\alpha_{4,z})[\sin(-\alpha_{4,z})\tan\alpha_2 + \cos(-\alpha_{4,z})]\right\} - [P_1(x,z)+P_2(x,z)](\sin\beta + \cos\beta\tan\alpha_2)}{2\cos\alpha_1\tan\alpha_2 - \sin\alpha_1} + \frac{Q(x,z)f_{cs}z + [P_1(x,z)-P_2(x,z)]\sin\alpha_{11}z_P + \left\{Q(x,z)\cos(-\alpha_{4,z})z - [P_2(x,z)-P_1(x,z)]\cos\alpha_{11}z_P\right\}\tan(\alpha_2+\alpha_{4,z})}{2[\cos(\alpha_1+\alpha_{4,z})z_F\tan(\alpha_2+\alpha_{4,z}) - \sin(\alpha_1+\alpha_{4,z})z_F]} \quad (43)$$

In light of Equations (42) and (43), the loading characteristic of the front connecting rod associated with the right pillar can be described as

$$F_1(x,z) = \frac{Q(x,z)\left\{\tan\alpha_2 + f\cos(-\alpha_{4,z})[\sin(-\alpha_{4,z})\tan\alpha_2 + \cos(-\alpha_{4,z})]\right\} - [P_1(x,z)+P_2(x,z)](\sin\beta + \cos\beta\tan\alpha_2)}{2\cos\alpha_1\tan\alpha_2 - \sin\alpha_1} - \frac{Q(x,z)f_{cs}z + [P_1(x,z)-P_2(x,z)]\sin\alpha_{11}z_P + \left\{Q(x,z)\cos(-\alpha_{4,z})z - [P_2(x,z)-P_1(x,z)]\cos\alpha_{11}z_P\right\}\tan(\alpha_2+\alpha_{4,z})}{2[\cos(\alpha_1+\alpha_{4,z})z_F\tan(\alpha_2+\alpha_{4,z}) - \sin(\alpha_1+\alpha_{4,z})z_F]} \quad (44)$$

Furthermore, the loading characteristic on the rear rod corresponding to the left pillar can be expressed as

$$F_2(x,z) = \frac{Q(x,z) + fQ(x,z)\cos(-\alpha_{4,z})\sin(-\alpha_{4,z}) - [P_1(x,z)+P_2(x,z)]\cos\beta - F_1(x,z)\cos\alpha_1}{\cos\alpha_2} - \frac{Q(x,z)f_{cs}z + [P_1(x,z)-P_2(x,z)]\sin\alpha_{11}z_P + \left\{Q(x,z)\cos(-\alpha_{4,z})z - [P_2(x,z)-P_1(x,z)]\cos\alpha_{11}z_P\right\}\tan(\alpha_1+\alpha_{4,z})}{2[\cos(\alpha_2+\alpha_{4,z})z_F\tan(\alpha_1+\alpha_{4,z}) - \sin(\alpha_2+\alpha_{4,z})z_F]} \quad (45)$$

Meanwhile, the loading characteristic on the rear rod corresponding to the right pillar is:

$$F_2'(x,z) = \frac{Q(x,z) + fQ(x,z)\cos(-\alpha_{4,z})\sin(-\alpha_{4,z}) - [P_1(x,z)+P_2(x,z)]\cos\beta - F_1(x,z)\cos\alpha_1}{\cos\alpha_2} + \frac{Q(x,z)f_{cs}z + [P_1(x,z)-P_2(x,z)]\sin\alpha_{11}z_P + \left\{Q(x,z)\cos(-\alpha_{4,z})z - [P_2(x,z)-P_1(x,z)]\cos\alpha_{11}z_P\right\}\tan(\alpha_1+\alpha_{4,z})}{2[\cos(\alpha_2+\alpha_{4,z})z_F\tan(\alpha_1+\alpha_{4,z}) - \sin(\alpha_2+\alpha_{4,z})z_F]} \quad (46)$$

7. Base Responsiveness Characteristics

Considering the force balance along the vertical, taking the upward direction as positive, the expression can be presented as

$$Q_V(x,z) - fQ_v(x,z)\cos\alpha_{1,z}\sin\alpha_{1,z} - P(x,z)\cos\beta - F_1(x,z)\cos\alpha_1 - F_2(x,z)\cos\alpha_2 = 0 \quad (47)$$

where Q_v refers to the vertical load on the base. $\alpha_{1,z}$ denotes the coupling angle between base and base plate. P is working resistance of the column.

In light of the principle of load equilibrium, the horizontal force can be defined as the resultant force after subtracting the opposing frictional force. When the value is positive, it implies a right-ward direction. This logical relationship can be inferred from the equation below:

$$-Q_H(x,z) - f_1Q_V(x,z)\cos\alpha_{1,z}\cos\alpha_{1,z} + P(x,z)\sin\beta - F_1(x,z)\sin\alpha_1 - F_2(x,z)\sin\alpha_2 = 0 \quad (48)$$

$$\begin{cases} Q_V(x,z) = \frac{P(x,z)\cos\beta + F_1(x,z)\cos\alpha_1 + F_2(x,z)\cos\alpha_2}{1 - f\cos\alpha_{1,z}\sin\alpha_{1,z}} \\ Q_H(x,z) = P(x,z)\sin\beta - F_1(x,z)\sin\alpha_1 - F_2(x,z)\sin\alpha_2 - f_1Q_V(x,z)\cos\alpha_{1,z}\cos\alpha_{1,z} \end{cases} \quad (49)$$

where f_1 denotes the friction coefficient between the base and the bottom plate. $\alpha_{1,z}$ refers to the angle of the base. Q_H signifies the horizontal load on the base.

The moment expression concerning point O' is written as

$$r_1P(x,z) - \left\{ \begin{array}{l} [Q_H(x,z) + fQ_V(x,z)\cos\alpha_{1,z}\cos\alpha_{1,z}][y_{O'} + (L_{OM} - X')\sin\alpha_{1,z}] \\ +[Q_V(x,z) - fQ_V(x,z)\cos\alpha_{1,z}\sin\alpha_{1,z}][x_{O'} + (L_{OM} - X')\cos\alpha_{1,z}] \end{array} \right\} = 0 \quad (50)$$

Considering the base as the research object, the moment expression perpendicular to the direction of the base concerning the XOY plane is expressed as

$$\left\{ \begin{array}{l} [Q_V(x,z)\cos(\alpha_{1,z}) + Q_H(x,z)\sin(\alpha_{1,z})]z_B \\ +[P_1(x,z) - P_2(x,z)]\cos\beta_{11}z_P \end{array} \right\} + \left\{ \begin{array}{l} [F_1(x,z) - F_1'(x,z)]\cos\beta_{22}z_F \\ +[F_2(x,z) - F_2'(x,z)]\cos\beta_{33}z_F \end{array} \right\} = 0 \quad (51)$$

where β_{11} represents the vertical inclination angle of the base, defined as the angular separation between the column and the base. β_{22} signifies the attitude of the front linkage relative to the base in the vertical direction while β_{33} represents the vertical attitude of the rear linkage relative to the base. The resultant force on the base can be obtained from the following equation. z_F is the length of the front and rear connecting rods in the Z-axis direction. z_B denotes the represents the position of the base load in the Z-axis direction.

$$\begin{cases} X'(x,z) = L_{OM} - \dfrac{[P_1(x,z)+P_2(x,z)]r_1 - \left\{ \begin{array}{l} [Q_H(x,z) + fQ_V(x,z)\cos\alpha_{1,z}\cos\alpha_{1,z}]y_{O'} \\ +[Q_V(x,z) - fQ_V(x,z)\cos\alpha_{1,z}\sin\alpha_{1,z}]x_{O'} \end{array} \right\}}{\left\{ \begin{array}{l} [Q_H(x,z) + fQ_V(x,z)\cos\alpha_{1,z}\cos\alpha_{1,z}]\sin\alpha_{1,z} \\ +[Q_V(x,z) - fQ_V(x,z)\cos\alpha_{1,z}\sin\alpha_{1,z}]\cos\alpha_{1,z} \end{array} \right\}} \\ z_{Base}(x,z) = \dfrac{\left\{ \begin{array}{l} [Q_V(x,z)\cos(\alpha_{1,z}) + Q_H(x,z)\sin(\alpha_{1,z})]z_B \\ +[P_1(x,z) - P_2(x,z)]\cos\beta_{11}z_P \end{array} \right\} + \left\{ \begin{array}{l} [F_1(x,z) - F_1{}'(x,z)]\cos\beta_{22}z_F \\ +[F_2(x,z) - F_2{}'(x,z)]\cos\beta_{33}z_F \end{array} \right\}}{Q_V(x,z)\cos(\alpha_{1,z}) + Q_H(x,z)\sin(\alpha_{1,z})} \end{cases} \quad (52)$$

where X' represents the position of the load, which is applied in the X-axis direction.

Initially, the forward Kinematics model of ZY1000/08/15 hydraulic support is developed using the D-H theory [60]. The position space transformation from the driving space is determined by efficiently extending the drive units, and the space mutual transformation is carried out on the Matlab platform (R2016a). Thereafter, the known working expansion of the drive units determines the shield support concerning posture. The analysis of the support's performance then involves determining the boundary conditions using the balanced working pressure and the known left and right columns. Furthermore, it is possible to determine the bearing performance of the support. Finally, further calculations are displayed for evaluating the behavior of the support using Equations (47) and (48). The scheme of Matlab is shown in Figure 3.

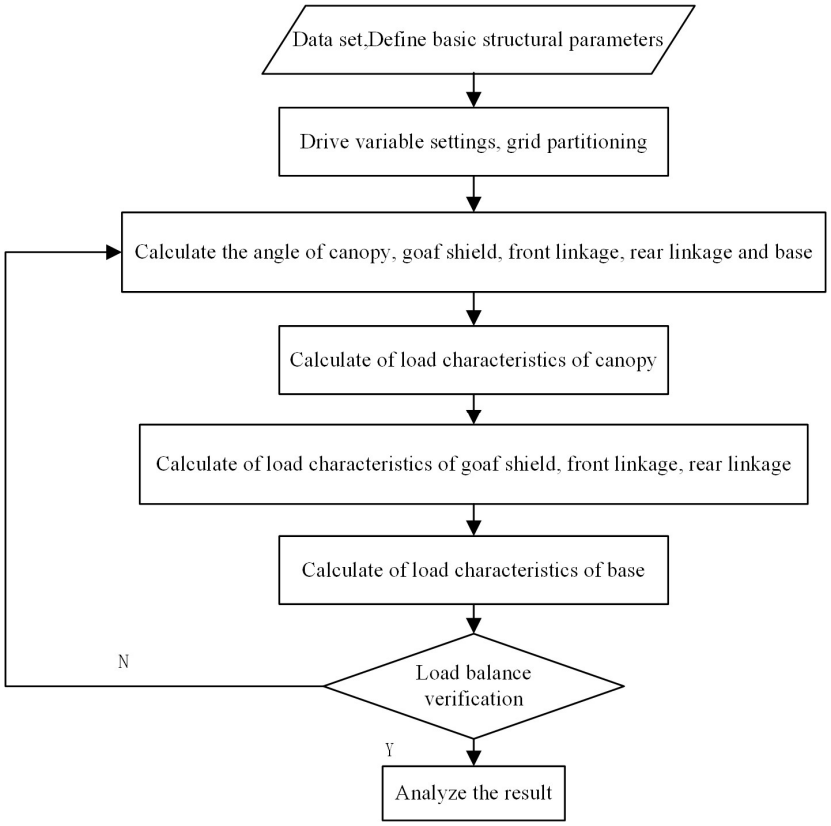


Figure 3. Scheme of Matlab.

8. Computational Scheme

The types of CPU and graphics card are 12th Gen Intel(R) Core(TM) i7-12700F 2.10 GHz and NVIDIA GeForce RTX 3060 (12 GB), which are employed by investigating the loading characteristics of the hydraulic support. The calculation cycle of the proposed model based on the personal computer configuration mentioned above is less than 2.3 s, which fully satisfies the requirements for the underground operation cycle of hydraulic supports. When taking into account the load-bearing characteristics of hydraulic supports, particularly those linked to the load-bearing capacity of the canopy, a strong correlation exists between these factors and the posture of the canopy as well as the real-time working pressure of the drive units. The calculation flowchart of hydraulic support bearing characteristics under three-dimensional spatial conditions is depicted in Figure 4, with the following specific steps:

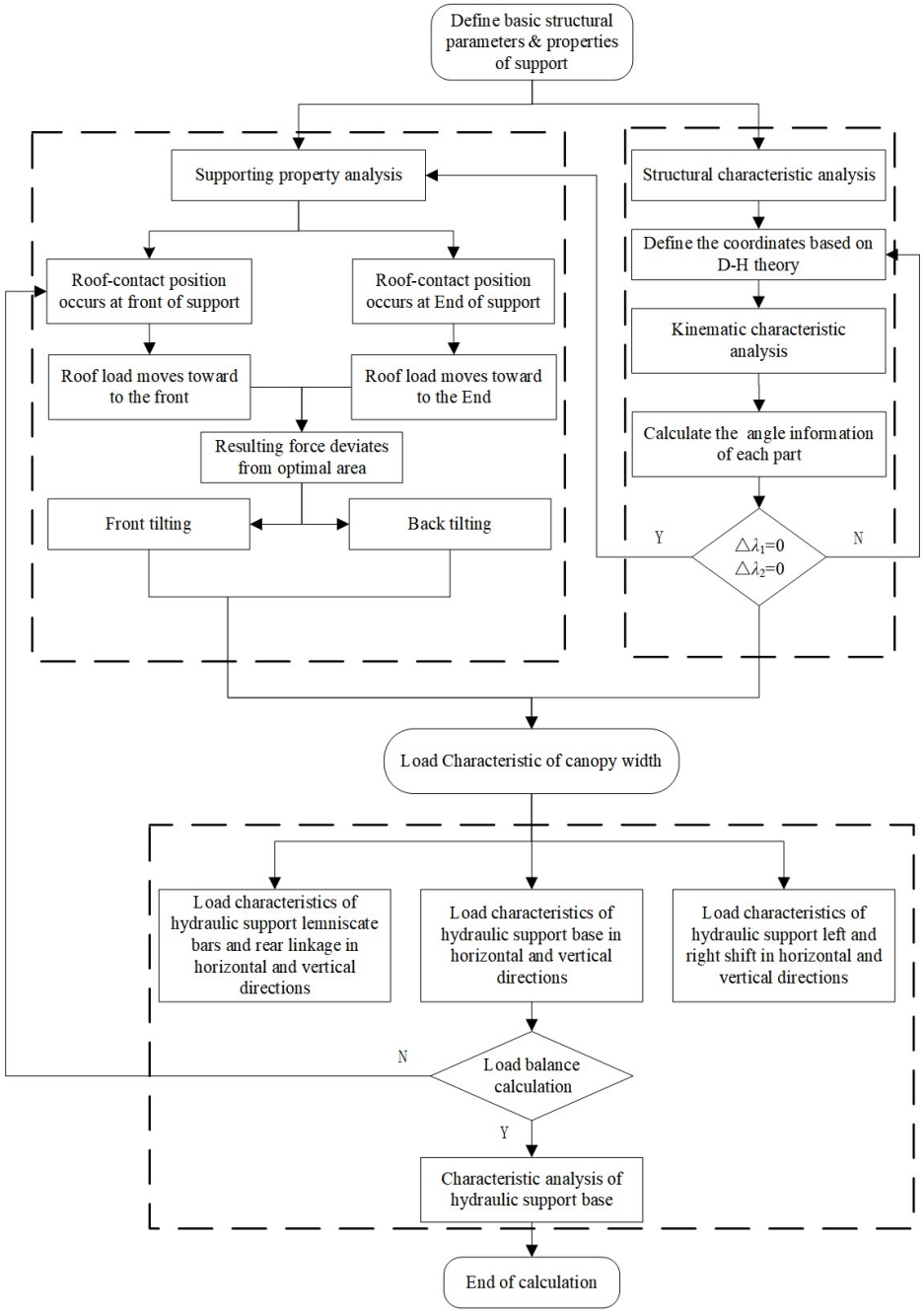


Figure 4. Computational flowchart.

To validate the established model, a verification process was performed considering mechanical equilibrium along the X- and Y-directions. Taking the entire hydraulic support as the target analysis object, the external loads of the top beam and base calculated based on Equation (1) to Equation (52), serve to confirm the resultant loading state in the *X*-axis and *Y*-axis directions. In the event that the loading state achieves equilibrium, it provides evidence that the calculation process of the mathematical model presented in this paper is trustworthy. Figure 5 illustrates the three-dimensional spatial results along the vertical and horizontal directions. It has been observed that the error orders of moment calculation in the absolute coordinate system are less than 10^{-10} due to the roundings in calculations, which is in good accordance with the calculation requirements. The maximum value on the length and width direction of the powered support appeared to be fully acceptable. Moreover, a verification using the coupling simulation model was carried out.

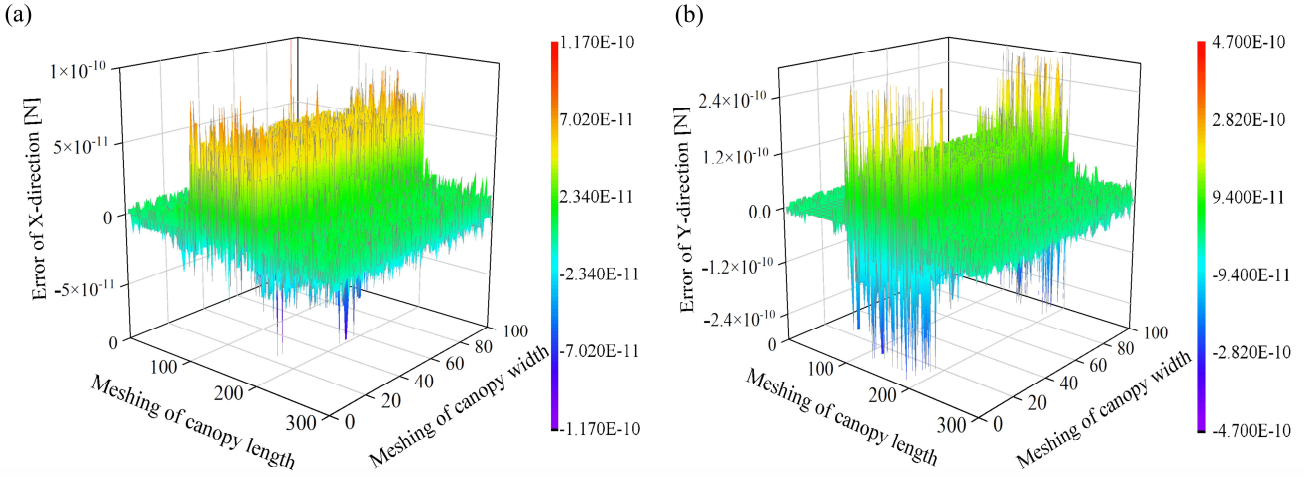


Figure 5. Model verification: errors along (**a**) X-direction and (**b**) Y-direction.

The fluctuation of the bearing properties of the canopy throughout the length and width directions is shown in Figure 6. The effective elongation of the column was found to be 675.4 mm, while that of the equilibrium jack was found to be 21.2 mm. The frictional coefficient between the immediate roof and canopy was set to 0.3 [60]. Figure 5 depicts the bearing performance of the canopy model. The hydraulic support canopy demonstrated its highest load capacity at the position of its symmetrical plane, gradually decreasing from the center position to both sides. Consequently, the shield support attains its maximum load-bearing capacity when the load is accurately placed on the plane of central symmetry of the shield support. The width of the canopy of the support decreases monotonically in a parabolic shape, with the lowest load capacity at both ends, which is less than one-fifth of the load capacity of the neutral plane of the support. The working range of the equilibrium jack for tension and compression has a lower loading property than the working range for columns. With the strongest load capacity within the effective load range, the column working range represents the ideal working range for the carrying characteristic of the support, which is consistent with Meng [47].

Figure 7 illustrates the load properties of the canopy in terms of length and width directions when the drive units were fixed at 1345.4 mm and 419.2 mm, and the canopy and immediate roof showed a friction coefficient of 0.3. The loading characteristics were found to be symmetrically distributed in the width direction, with the central position having the largest load capacity and the other positions having progressively less load capacities. Meanwhile, the optimal load area is identified in the column working area within the neutral plane area. The load curve distribution of the canopy follows the same trend as the two-dimensional spatial load distribution in Figure 7b. In general, the stress

distribution throughout the working zone of the well-balanced jack shows an increasing tendency. There is a progressive decrease within the vertical work region along the canopy axis. As the equilibrium jack moves swiftly along the length of the canopy within the compressed zone, its load-bearing capacity gradually decreases from the center towards both ends.

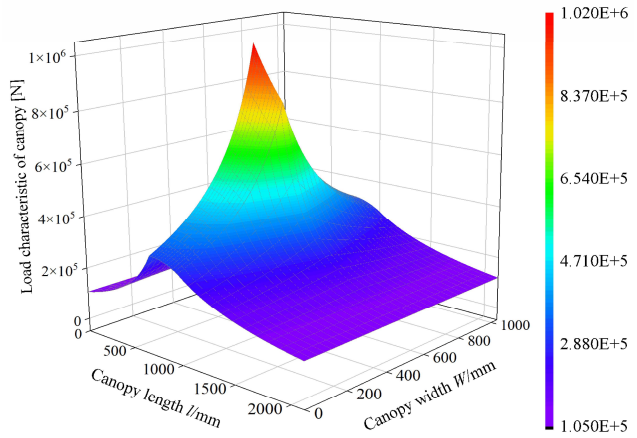


Figure 6. Carrying characteristics of the canopy model.

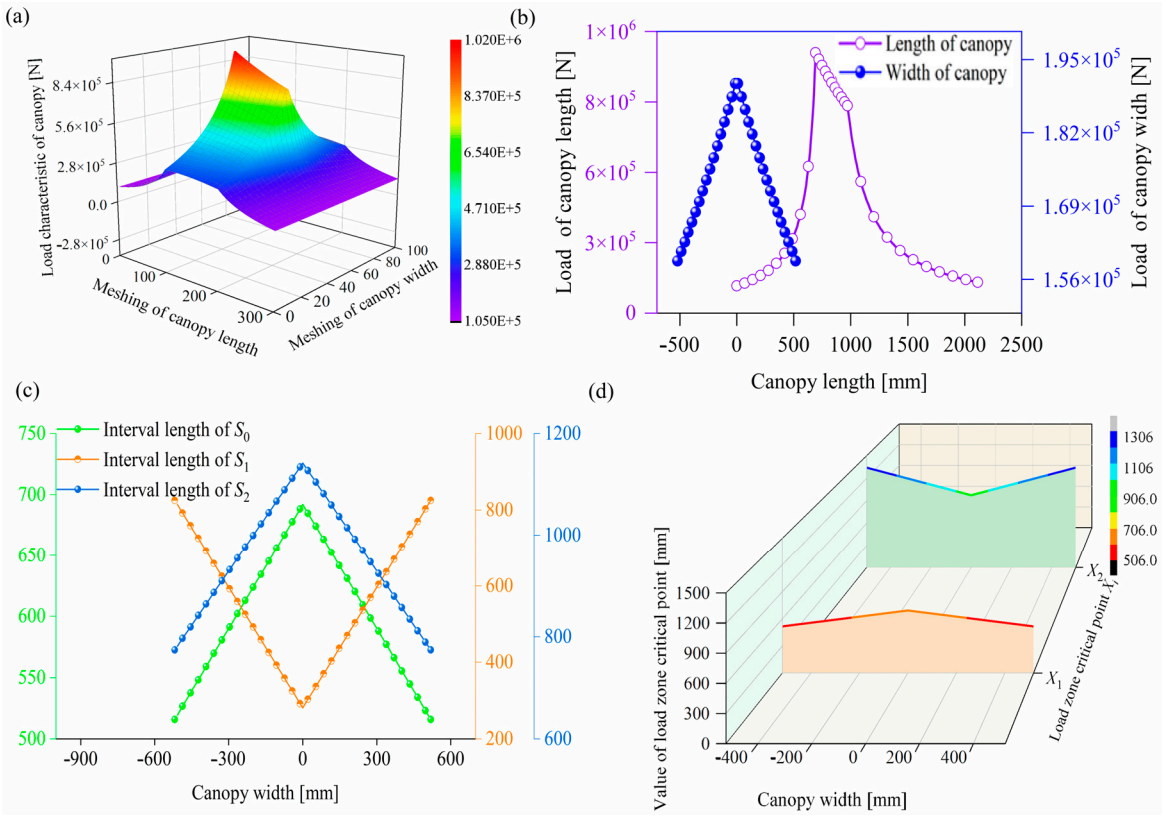


Figure 7. (**a**) Carrying characteristics of the canopy. (**b**) Critical point changes along the support width. (**c**) Variations in the length of the working interval. (**d**) Values at the critical point.

Figure 7c displays a variation curve concerning the tension working area, column working area, and that of the equilibrium jack along the canopy width direction. S_0 denotes the extent of the equilibrium jack tension working region, S_1 signifies the elongation of the column working region, and S_2 indicates the measurement of the compression working region in the equilibrium jack. It was found that in the direction of the canopy's width, the effective lengths of S_0 and S_2 initially increased and subsequently decreased, whereas

the effective length of S_1 initially decreased and subsequently increased. This conclusion implies that the effective working range of the column reaches the maximum value at both ends and lowest value in the middle along the canopy width direction. The working area of the equilibrium jack for tension and compression is the longest in the middle and lowest on each side.

Figure 7d presents the boundary points of the column work area along the support width. It reveals a noticeable shift in the position of the initial point (X_1) within the working area of the pillar as the canopy width increases. This shift involves an initial movement towards the coal wall direction, followed by a gradual transition towards the goaf. Moreover, the position (X_2) of the termination point of the pillar working area first decreases and then increases, indicating that X_2 first moves towards the goaf and then gradually moves towards the coal wall direction.

Figure 8 illustrates the carrying characteristics of the rear- and front-lingkage. The graph reveals an opposite trend in the changes in the left and right front connecting rods. Specifically, when the load on the left front connecting rod is larger, the load on the right connecting rod is smaller. Furthermore, when the left front link is subjected to tension, the right front link is under compression. This phenomenon primarily stems from the symmetrical structure of the left and right connecting rods. When the bracket is in an off-center state, the symmetrically arranged left and right front connecting rods display distinct load states. The above observations suggest that the left and right front connecting rods experience their maximum load within the column's working area, while the highest pressure is encountered at the support edge.

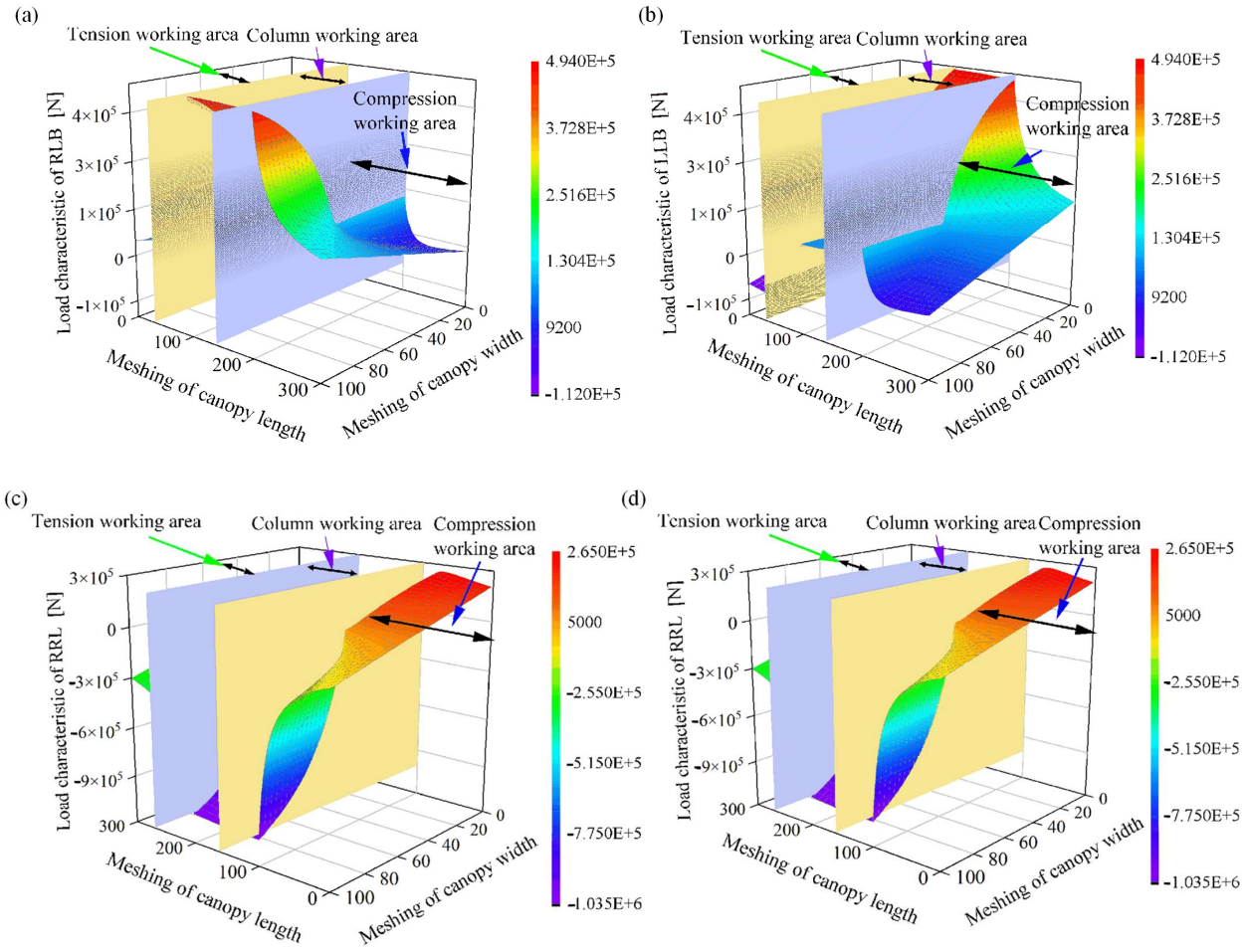


Figure 8. Carrying characteristics of the four connecting bars: (**a**) left front linkage; (**b**) right front linkage; (**c**) left rear linkage; (**d**) right rear linkage.

The load-bearing characteristics of the four-link mechanism are plotted in Figure 8c,d. It is observed that as the load on the left rear linkage increases, the corresponding load on the right rear linkage reduces. It is inferred that the loading characteristic on the front rods and rear rods at both ends along the neutral plane increases along the canopy width, primarily due to the presence of eccentric load. Consequently, the lowest load performance occurs near the neutral plane of the support's canopy, which is advantageous for the supporting behavior at the rear and front linkages.

Figure 9 illustrates the pressure distribution at the front and back ends of the base. The convex profile of the front-end specific pressure along the canopy width direction indicates that the support base is positioned backward. The primary explanation for this observation is the effect of eccentric load. The neutral plane is the best place to sustain the front-end pressure ratio of the base.

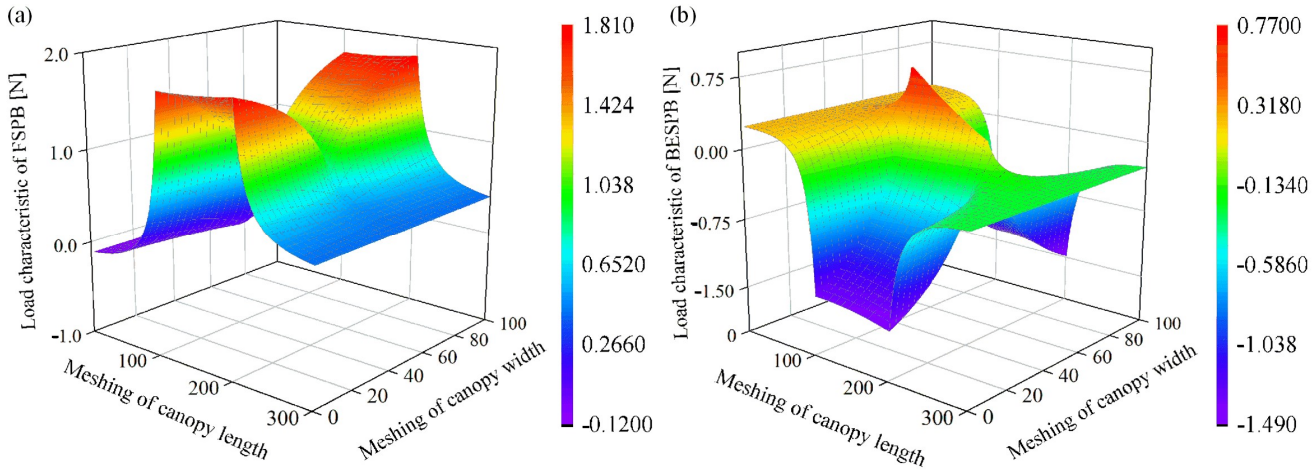


Figure 9. Distribution of the base pressure: (**a**) front-end pressure; (**b**) back-end pressure.

The rear end specific pressure of the base is plotted along the length and width directions of the canopy in Figure 9b. A reduction is followed by an improvement along the canopy width, indicating that the rear-end pressure distribution of the base is similar to the front-end pressure distribution. The majority of base postures are shown to be bottom-up, suggesting that the neutral plane position has the lowest bottom-up danger.

The comparison of Figure 9a,b demonstrates that the maximum positions of the front and rear specific pressure of the base occur at both ends of the support width. Meanwhile, the hydraulic support is confronted with the greatest risk of the base inclining forward and backward. On the other hand, the neutral surface of the shield support can be characterized as the place where the front and rear specific pressures attain their lowest values. This state of operation is favorable to the steady support of the shield support. Therefore, it is essential to guarantee that the working area of the column is in an optimal state and that the inter-active zone of the combined external load acts upon the neutral plane during the subterranean support operation.

Figure 10 shows the impact of different column working resistances on the canopy load when the expansion and contraction of the drive units were set to 21.2 mm and 675.4 mm, respectively. It is evident from Figure 10b that a higher operating pressure of the column leads to a better canopy loading performance concerning the initial and termination points of the column regarding the canopy width. Meanwhile, the initial point load is higher than that of the termination point. The fluctuation of the starting and ending point positions of the column with respect to the operating pressure of the column is shown in Figure 10c along the canopy width direction. It is also evident from the figure that when the initial action point of the column is closer to the direction of the coal wall the operating pressure

of the column becomes high, whereas the termination point of the pillar travels in the other direction, towards the goaf. The variation in the tension working area, column working area, and pressure working area with the operating pressure of the column is shown in Figure 10d. A longer effective working period of the tension and compression working areas is observed to be introduced by a higher working resistance of the column. However, the working range of the column exhibits a different pattern. The overall trend of change is similar to those reported by Yuan [60]. It can be explained by the operating pressure increasing of the column, which causes loads to increase both parallel to and perpendicular to the top beam. The carrying qualities of the support show a positive correlation with the operating pressure of the column, despite the decreasing efficacious range of the column. The loading capacity is thereby greatly increased by suitably enhancing the operating pressure of the column, which is similar to the variation law of Zhou [64].

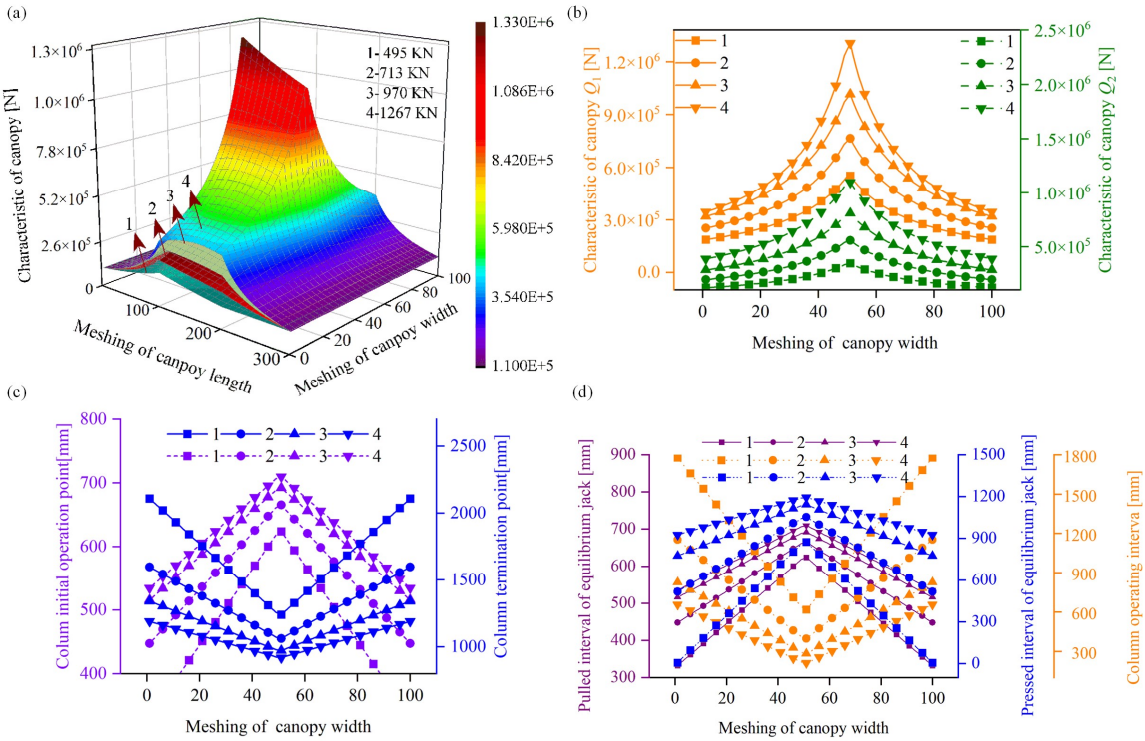


Figure 10. Effect of the column working resistance on load characteristics of canopy: (**a**) distribution of the canopy under different pressures; (**b**) load characteristics of the canopy; (**c**) initial critical point position X_1 of the column; (**d**) working interval length.

Figure 11 illustrates the impact of different equilibrium jack working resistances on the load behavior of the canopy when the elongation of the drive units was 21.2 mm and 675.4 mm. Figure 11a displays the load-bearing behavior of the canopy along the length and width direction versus equilibrium jack working resistances, while Figure 11b demonstrates that the changes in the canopy carrying properties are associated with the starting and concluding positions of the column's operational scope, considering the operating pressure of the equilibrium jack. The bearing characteristics corresponding to the initial and terminal points demonstrate an inverse relationship with the operating pressure of the equilibrium jack, and the above changes are similar to the research conclusions of Meng [47]. Figure 11c illustrates that increasing the operating pressure of the equilibrium jack causes the beginning position of the column to move closer to the coal wall while the endpoint also travels in that direction. The tension and compression working range of the equilibrium jack demonstrates a negative trend with the working resistance, as shown in Figure 11d, while the column displays a synchronous trend.

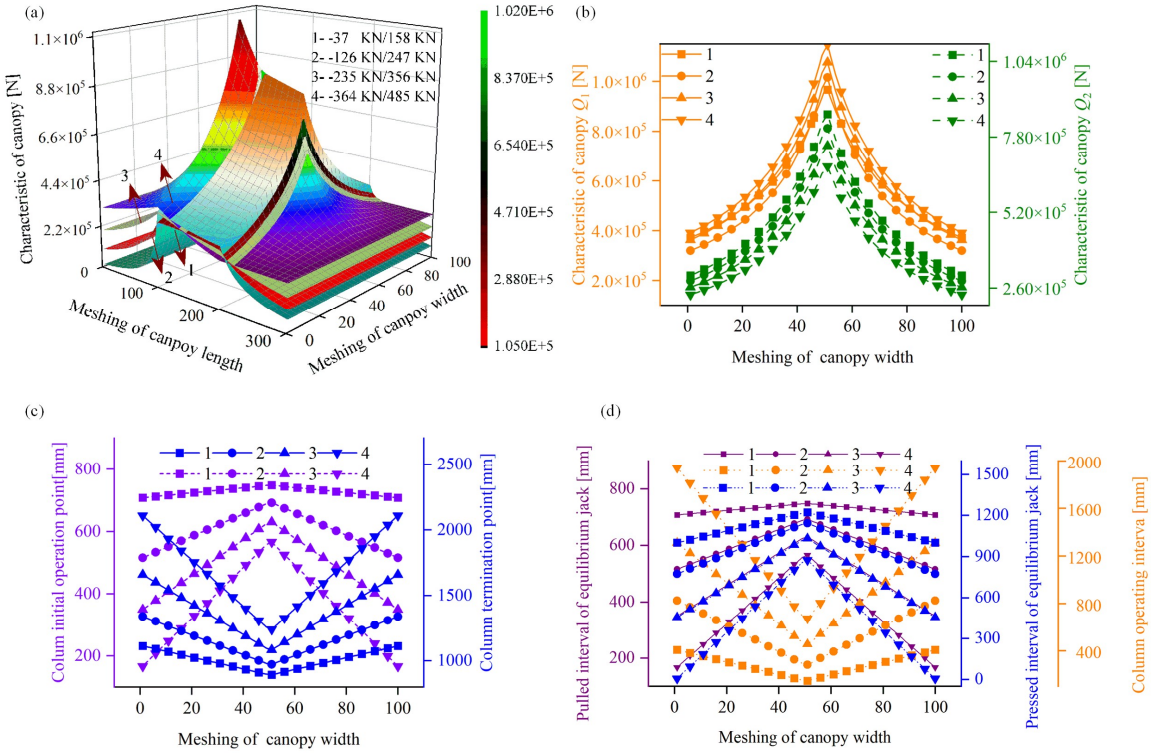


Figure 11. Effect of the equilibrium jack working resistance on canopy load behaviors: (**a**) distribution of the canopy under different pressures; (**b**) load characteristics of the canopy; (**c**) initial critical point position X1 of the column; (**d**) working interval length.

On the other hand, the maximum bearing performance of the equilibrium jack displays a different pattern, the canopy loading behavior develops as the operating pressure of the equilibrium jack improves. As evidenced by Yuan [60] findings, the operating pressure of the canopy during the tension and compression working intervals of the equilibrium jack demonstrates an inverse pattern with increasing equilibrium jack working resistance. The results of Figure 11 show that lengthening the operating resistance of the equilibrium jack has a positive loading effect on the working range of the column. The bearing performance of the canopy and the effective working interval of the column with regard to the hydraulic support can both be improved by a sensible design of the operating pressure of the equilibrium jack.

9. Experimental Work

9.1. Experimental Arrangement

To verify the correctness of the mathematical model proposed in this paper, a multifunctional hydraulic support experimental system is developed to measure the pose and load states of the hydraulic support. The testing model selected for this experimental platform is ZY1000/08/15, which is a hydraulic support designed with an elongated hydraulic support and scaled down proportionally.

Figure 12 shows the relationship diagram of the hydraulic support multifunctional test bench, including the test bench, the liquid supply system, and the hydraulic support. Among the various parts, the liquid supply system serves to be partitioned into an emulsion pump station and a hydraulic pump station, each with its own specific functions. The emulsion pump station predominantly undertakes the task of supplying liquid to the hydraulic support, while the hydraulic pump station is responsible for providing liquid to the diverse oil cylinders within the multifunctional loading test bench. The test bench encompasses an angle adjustment module, a plug-in pin positioning module, pressure sensors, displace-

ment sensors, and tilt-angle sensors. The test bracket is equipped with pressure sensors, displacement sensors, and inclination sensors. The hydraulic support measurement and control system is responsible for the collection, processing, and presentation of data.

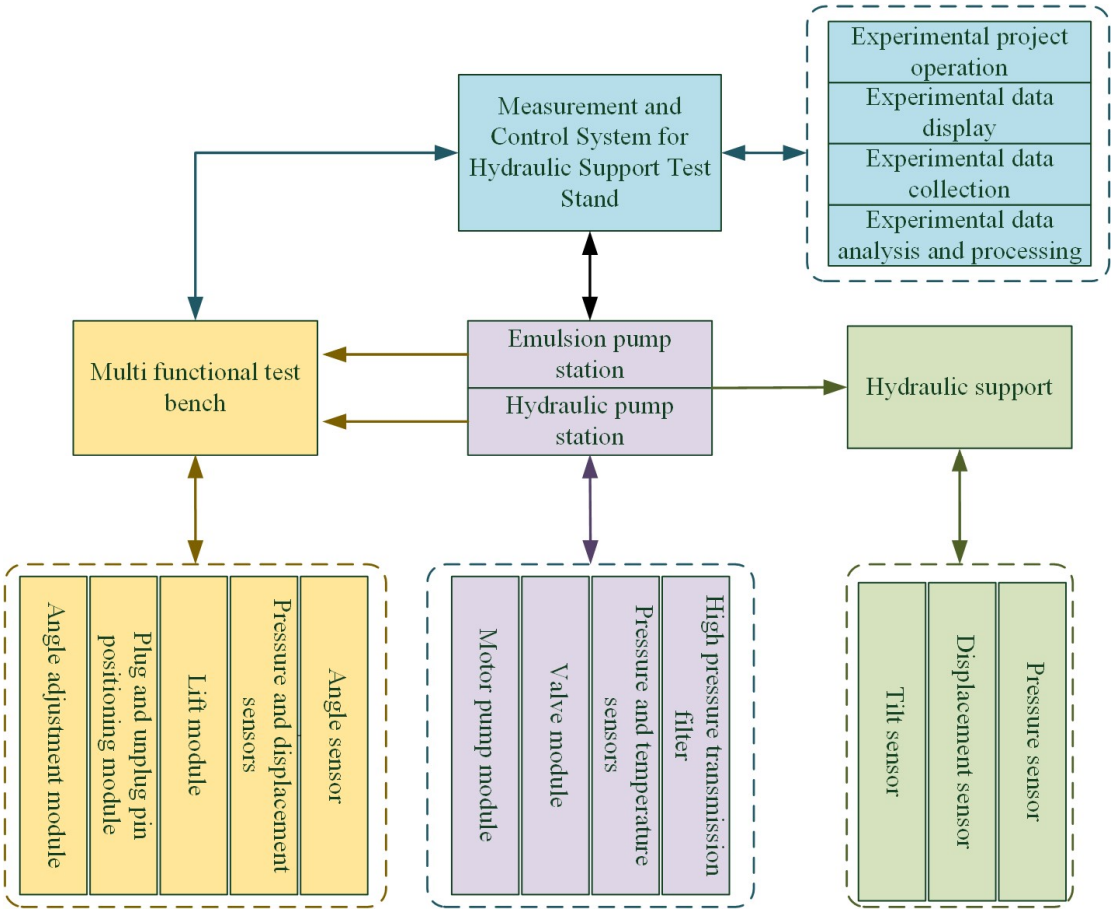


Figure 12. Structural diagram of multifunctional test bench.

Based on the independently developed multifunctional hydraulic support test bench and ZY1000/08/15 support shield hydraulic support as the test objects, a testing system is composed, as shown in Figure 13. The main components are the control unit, experimental unit, acquisition unit, and angle adjustment unit. The control unit includes an emulsion pump station, a hydraulic pump station, a multifunctional control console, and hydraulic pipelines. The testing unit is ZY1000/08/15 hydraulic support. In addition to the multifunctional hydraulic support acquisition system, the acquisition unit also includes an INV3060S acquisition system, two KSM58-J type wire sensors, an LZR-300-U laser displacement sensor, and a computer (PC), as shown in Table 3. The INV3060S data acquisition instrument performs data acquisition for the wire sensor and the laser displacement sensor. The INV3060S acquisition system, a high-precision data acquisition tester featuring 16 channels and 24-bit accuracy, undertakes signal transmission and acquisition tasks. The KSM58-J type cable sensors are, respectively, installed on the column and the balance jack, responsible for measuring the extension length of the column and the balance jack. The device features a measuring range reaching up to 1000 mm and a remarkable repeatability accuracy of ±2 BIT. The LZR-300-U laser displacement sensor is mounted on the side of the top beam and tasked with measuring the real-time support height of the bracket. It has a measuring range of 3000 mm and a reproducibility of 1 mm. The angle adjustment of the top plates of the multifunctional loading test bench is realized by controlling the liquid supply of the pump station via the multifunctional operation console.



Figure 13. Experimental apparatus.

Table 3. Required test equipment.

Selected Device Name	Model Specifications	Equipment Measurement Accuracy	Equipment Measurement range
Acquisition system	INV3060S (which is manufactured by Beijing Oriental Institute of Vibration and Noise Technology located in Beijing, China)	24 bits	/
Pullwire sensor	KSM58-J (which is manufactured by Shanghai Kangqiao Electronic Technology Co., Ltd. in Shanghai, China)	±2 BIT	1000 mm
Laser displacement sensor	LZR-300-U (which is manufactured by Shanghai Kangqiao Electronic Technology Co., Ltd. in Shanghai, China)	1 mm	3000 mm
Wired tilt sensor	SVT620T (which is manufactured by Maike Sensing Technology Co., Ltd. in Wuxi, China)	0.01°	180°

9.2. Experimental Results

As shown in Figure 14, When the expansion amounts of the column and the balance bar are 456.5 mm and 74 mm, respectively, the test curves of the test points are under four different loading pressures of 10.3 MPa, 15.3 MPa, 19.6 MPa, and 24.0 MPa. As depicted in Figure 14, there is a synchronous increase in the load on the canopy as the working pressure of the column rises. Meanwhile, it is evident that the average relative

error of the system is 9.08% when compared with the experimental results. Consequently, upon verification through this experiment, the proposed numerical model for predicting the load characteristics of hydraulic support top beams can be regarded as a reliable mathematical approach.

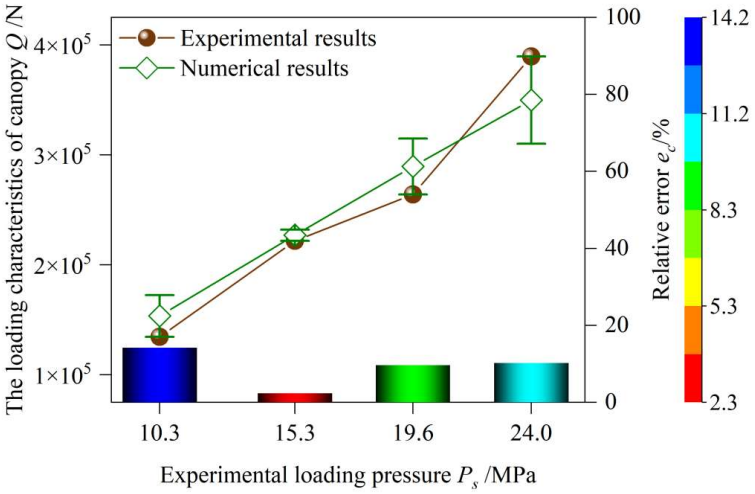


Figure 14. The canopy loading characteristics comparison between the simulation and experiment.

10. Conclusions

An innovative three-dimensional mathematical–physical model for evaluating load-carrying characteristics of powered support was constructed using the D-H forward kinematics model. This enabled the interactive monitoring of posture and load characteristics. The suggested approach was devised to investigate the bearing patterns of hydraulic support and experimentally verified. The modeling method proposed in this article has a wide range of applicability, and can be applied to both double-column shield hydraulic supports and four-column shield hydraulic supports, providing technical support for the development of intelligent underground coal mines. Some attractive characteristics of the developed hydraulic support are as follows.

(1) The load capacity at both ends is less than one-fifth of the load at the neutral plane, and the canopy load at both ends experiences a significant reduction along the neutral plane along the support width. The bearing performance of the front and rear links, as well as the pin shaft, significantly increases when the canopy load gradually moves towards both ends along the neutral plane. This exacerbates the risk of the hydraulic support base tilting forward and backward, which is unfavorable for stable underground support.

(2) The tension and compression working regions of the equilibrium jack have longer effective lengths at both ends, whereas the working section of the column gradually gets shorter along the neutral direction of the canopy. The action value of the termination point progressively approaches the coal wall, while the initial value of the working interval of the column approaches the goaf at both ends. Maintaining the combined force of the load as spread throughout the working range of the column and as close to the neutral plane of the canopy as feasible is an essential aspect of the hydraulic support function. As a result, the support operation becomes more reliable and secure, and the guarantee of its ideal load-carrying characteristics is achieved.

(3) Along the support width, the left and right front connecting rods demonstrate opposite change trends. When the front connecting rod on the left endures compression, the front connecting rod on the right also faces compression. This contrast is most pronounced in the working area of the column. However, in both the front and rear sections of the canopy, the difference between the four-link mechanism gradually decreases, ulti-

mately approaching linear change. The load of the two linkages shows opposite changes, and the variation pattern of the four-link mechanism often corresponds with that of the front linkages.

(4) The specific pressure of the base gradually increases along the neutral direction at both ends of the support width. With the majority of the front end in a span bottom state and the rear end in a raised bottom state, the front and rear ends are in opposing support states. Both ends of the base experience their maximum specific pressure, which is detrimental to steady support. To mitigate the likelihood of excessive specific pressure occurring during the support operation, it is crucial to ensure that the resultant force of the load is distributed within the operational scope of the column.

(5) The load-bearing characteristics of the support canopy are closely correlated with the operational resistance of the column. The maximum weight on the canopy is greatly increased when operational resistance increases, but the effective operating span of the column is likewise reduced. The working position of the pillar changes as the working resistance rises, with its end point moving closer to the goaf and the initial point within its operating range moving nearer the coal wall. This leads to an increase in the equilibrium jack's tension and compression ranges and a decrease in the effective span for column operation.

(6) The operational pressure of the equilibrium jack directly affects the load applied to the canopy. Improving the operational resistance of the equilibrium jack results in a minor increase in the bearing capacity of the canopy. The beginning action position of the column working section advances in the direction of the goaf, and the action position of the termination point moves in the direction of the coal wall. However, the increased loading behavior of the support is the result of a shorter effective equilibrium jack length concerning the tension and compression working sections. It highlights that the loading behavior of the support might be enhanced by designing the operating resistance optimally.

11. Further Work

The establishment of a three-dimensional spatial stress model for the shield support has been made possible by the hydraulic support, which can be simplified to a rigid body. Nevertheless, this model does not account for the fact that several associated support mechanisms, especially the direct contact between the rock surrounding the canopy, may deform under strain. This contact can sustain large impact loads, which could cause the canopy to potentially deform in both the length and width dimensions, affecting the behavior of the support. During the coupling process between the hydraulic support top beam and the surrounding rock, it may cause deformation of the top beam, resulting in changes in the support posture and affecting the support characteristics of the hydraulic support. Moreover, additional research is necessary to fully comprehend the effect of elements like motion pair clearance in the two columns, structural size problems, and over-constrained driving on the hydraulic support system. In addition, integrating monitoring data with digital twin systems to provide technical support for the implementation of intelligent adaptive control integration as a research focus for the next step of work. Other influencing factors need to be considered, such as temperature variations, material fatigue, or hydraulic fluid dynamics, the mining and geological conditions of the walls, which might influence the performance of hydraulic supports in real-world scenarios.

Author Contributions: X.Y.: Conceptualization, methodology, software, data curation, writing—original draft preparation, supervision, writing—reviewing and editing. B.Y.: Project administration, Writing draft preparation. J.Z.: Software, Data curation. X.Z.: Writing- Original draft preparation, Software. Y.X.: Assisted laboratory analyses, writing—reviewing. All authors have read and agreed to the published version of the manuscript.

Funding: This research received funding from the National Natural Science Foundation of China [No. U1610251], and Scientific and Technological Innovation Programs of Higher Education Institutions in Shanxi [No. 2023L179], and Taiyuan University of Science and Technology Scientific Research Initial Funding [No. 20222115], and Excellent Doctor to Shanxi Research Funding Project [No. 20232070].

Institutional Review Board Statement: Not applicable.

Informed Consent Statement: Not applicable.

Data Availability Statement: The original contributions presented in this study are included in the article. Further inquiries can be directed to the corresponding author.

Conflicts of Interest: The researchers have disclosed no potential conflicts of interest in relation to the study, authorship, and/or publication of this article.

Nomenclature

b_c	mm	Distance from the instantaneous center of four-link mechanism to canopy
f	/	Friction coefficient between canopy and immediate top
f_1	/	Friction coefficient between base and bottom plate
F_1	N	Force on the left front rod
$F_{1'}$	N	Force on the right front rod
F_2	N	Force on the left rear rod
$F_{2'}$	N	Force on the right rear connecting rod
F_{1s}	N	Force on the left shaft
F_{2s}	N	Force on the right shaft
F_{1X}	N	Force on the left shaft parallel to canopy
F_{2X}	N	Force on the right shaft parallel to canopy
F_{1Y}	N	Force on the left shaft in the vertical direction of canopy
F_{2Y}	N	Force on the right shaft in the vertical direction of canopy
H_0	mm	the distance from the hinge position of goaf shield to the canopy
h_e	mm	Dstance of the equilibrium jack in the vertical direction of canopy
h_P	mm	Vertical distance between column and canopy
h_T	mm	distance from the junction point of equilibrium jack and canopy to the column
h_x	mm	Distance of shaft in the vertical direction of canopy
N_C	/	Column length node
N_E	/	Equilibrium jack length node
n_1	/	Canopy length direction divides the nodes
n_2	/	Canopy width direction divides the nodes
O'	/	Instantaneous hinge point of four rods
P	N	Working resistance of column
P_1	N	Operating pressure of left column
P_2	N	Operating pressure of right column
P_E	N	Operating pressure of equilibrium jack
P_L	N	Tension working resistance of equilibrium jack
P_{max}	N	Maximum operating pressure of column
P_Y	N	Compression working resistance of equilibrium jack
Q	N	Load of canopy
Q_{FX}	N	Load of X direction of shaft
Q_{FY}	N	Load of Y direction of shaft
Q_f	N	Load of front rod
Q_H	N	Load on the base in the horizontal direction
Q_V	N	Load on the base in the vertical direction
$Q_i_T_i$	N	Load in two different areas on the left or right
$Q_i_P_1$	N	Load corresponding to the force of left column of the ith working area

$Q_i_P_2$	N	Load corresponding to the force of right column of the ith working area
$Q_i_P_{1\max}$	N	Load corresponding to the operating pressure of left column of the ith working area
$Q_i_P_{2\max}$	N	Load corresponding to the operating pressure of right column of the ith working area
Q_i_T	N	Load corresponding to the effective interval of equilibrium jack of the ith working area
Q_r	N	Load of rear lenkage
Q_V	N	Load of the base in the vertical direction
r_1	mm	Vertical distance to the column between the shaft of canopy and the shield
r_2	mm	Vertical distance from O' point to column
t	mm	Vertical distance from point O' to equilibrium jack
x_P	mm	distance from the end of the canopy to the installation point of column
x_T	mm	distance from the end of canopy to the installation point of equilibrium jack
X'	mm	Position of base load
$x_{1_}\mathrm{P}_i$	mm	Boundary point between the tension working area of the equilibrium jack corresponding to the left and right columns and the working area of the columns.
$x_{2_}\mathrm{P}_i$	mm	Boundary point between the working area of the left and right columns and the compressed working area of the equilibrium jack
z_B	mm	Coordinate of the base load in the Z-axis direction
z_E	mm	Coordinate between equilibrium jack and canopy in the width direction
z_p	mm	Coordinate of the articulation point between column and canopy in the width direction of canopy
z_J	mm	Coordinate of the equilibrium in the width direction of canopy
z_x	mm	Coordinate of the shaft of canopy and the shield in the coordinate of the width direction of canopy
α_1	°	Inclination of the front linkage relative to the horizontal opposite
α_2	°	Inclination of the rear linkage relative to the horizontal opposite
$\alpha_{1,z}$	°	Coupling angle between base and base plate
$\alpha_{2,z}$	°	Attitude of rear linkage
$\alpha_{3,z}$	°	Attitude of shield goaf
$\alpha_{4,z}$	°	Coupling attitude of canopy relative to immediately roof
α_{11}	°	Vertical attitude of column relative to canopy
α_{22}	°	Angle between the equilibrium jack and the direction perpendicular to the canopy
β	°	Force acting on the left and right rear linkages
β_{11}	°	Vertical attitude between column and base in the base direction
β_{22}	°	Attitude between the front bar and base perpendicular to base
β_{33}	°	Attitude of the rear bar relative to base in the vertical direction of base
ψ	°	Angle between the instantaneous center of the four-link mechanism and the hinge position of the goaf shield and canopy, and the X-axis direction

References

1. Wang, G.; Xu, Y.; Ren, H. Intelligent and ecological coal mining as well as clean utilization technology in China: Review and prospects. *Int. J. Min. Sci. Technol.* **2019**, *29*, 161–169. [CrossRef]
2. Tian, Y.; Yang, X.; Yang, J.; Mao, K.; Yao, Y.; Liang, H. Evolution dynamic of intelligent construction strategy of coal mine enterprises in China. *Heliyon* **2022**, *8*, e10933. [CrossRef] [PubMed]
3. Zhang, K.; Kang, L.; Chen, X.; He, M.; Zhu, C.; Li, D. A Review of Intelligent Unmanned Mining Current Situation and Development Trend. *Energies* **2022**, *15*, 513. [CrossRef]
4. Zhang, Y.; Li, M.; Wang, B.; Yuan, J.; Tong, R. Developing a taxonomy and a dependency assessment model of performance influencing factors for intelligent coal mines. *Process Saf. Environ. Prot.* **2022**, *168*, 150–165. [CrossRef]
5. Li, S.; Xie, J.; Wang, X.; Mei, Z. MHDA-KD: A Multi-Granularity hybrid driven approach of Knowledge-Data for pose detection in complex dynamic operating system. *Expert Syst. Appl.* **2025**, *267*, 126227. [CrossRef]

6. Noy, S.; Zhang, W. Experimental evidence on the productivity effects of generative artificial intelligence. *Science* **2023**, *381*, 187–192. [CrossRef]
7. Samadi-Koucheksaraee, A.; Chu, X. Development of a novel modeling framework based on weighted kernel extreme learning machine and ridge regression for streamflow forecasting. *Sci. Rep.* **2024**, *14*, 30910. [CrossRef]
8. Samadi-Koucheksaraee, A.; Shirvani-Hosseini, S.; Ahmadianfar, I.; Gharabaghi, B. Optimization Algorithms Surpassing Metaphor. In *Computational Intelligence for Water and Environmental Sciences*; Bozorg-Haddad, O., Zolghadr-Asli, B., Eds.; Springer Nature: Singapore, 2022; pp. 3–33.
9. Fang, Y.; Ahmadianfar, I.; Samadi-Koucheksaraee, A.; Azarsa, R.; Scholz, M.; Yaseen, Z.M. An accelerated gradient-based optimization development for multi-reservoir hydropower systems optimization. *Energy Rep.* **2021**, *7*, 7854–7877. [CrossRef]
10. Ahmadianfar, I.; Heidari, A.A.; Gandomi, A.H.; Chu, X.; Chen, H. RUN beyond the metaphor: An efficient optimization algorithm based on Runge Kutta method. *Expert Syst. Appl.* **2021**, *181*, 115079. [CrossRef]
11. Ahmadianfar, I.; Bozorg-Haddad, O.; Chu, X. Gradient-based optimizer: A new metaheuristic optimization algorithm. *Inf. Sci.* **2020**, *540*, 131–159. [CrossRef]
12. Wang, G.; Wang, H.; Ren, H.; Zhao, G.; Pang, Y.; Du, Y.; Zhang, J.; Hou, G. 2025 scenarios and development path of intelligent coal min. *J. China Coal Soc.* **2018**, *43*, 295–305.
13. Mei, Z.; Wang, X.; Xie, J.; Li, S.; Liu, J. A sensing system and solving method for dynamic detection of relative pose of hydraulic support group. *Measurement* **2025**, *243*, 116145. [CrossRef]
14. Yang, Y.; Zhou, W.; Jiskani, I.M.; Wang, Z. Extracting unstructured roads for smart Open-Pit mines based on computer vision: Implications for intelligent mining. *Expert. Syst. Appl.* **2024**, *249*, 123628. [CrossRef]
15. Yang, B.; Yang, S.; Wang, P.; Wang, H.; Jiang, J.; Ni, R.; Yang, C. FRPNet: An improved Faster-ResNet with PASPP for real-time semantic segmentation in the unstructured field scene. *Comput. Electron. Agric.* **2024**, *217*, 108623. [CrossRef]
16. van der Gaast, N.; Bagave, P.; Assink, N.; Broos, S.; Jaarsma, R.L.; Edwards, M.J.R.; Hermans, E.; Ijpma, F.F.A.; Ding, A.Y.; Doornberg, J.N.; et al. Deep learning for tibial plateau fracture detection and classification. *Knee* **2025**, *54*, 81–89. [CrossRef] [PubMed]
17. Hadir, A.; Adjou, M.; Assainova, O.; Palka, G.; Elbouz, M. Comparative study of agricultural parcel delineation deep learning methods using satellite images: Validation through parcels complexity. *Smart Agric. Technol.* **2025**, *10*, 100833. [CrossRef]
18. Murray, L.; Castillo, T.; Martín de Diego, I.; Weber, R.; González-Olabarria, J.R.; García-Gonzalo, J.; Weintraub, A.; Carrasco-Barra, J. Deep reinforcement learning for optimal firebreak placement in forest fire prevention. *Appl. Soft Comput.* **2025**, *175*, 113043. [CrossRef]
19. Cheng, Q.; Ren, H.; Meng, X.; Li, A.; Xie, L. Real-time seismic response prediction method of high-rise buildings based on deep learning for earthquake early warning. *Int. J. Disaster Risk Reduct.* **2025**, *119*, 105294. [CrossRef]
20. Leng, B.; Gao, S.; Xia, T.; Pan, E.; Seidelmann, J.; Wang, H.; Xi, L. Digital twin monitoring and simulation integrated platform for reconfigurable manufacturing systems. *Adv. Eng. Inform.* **2023**, *58*, 102141. [CrossRef]
21. Zhang, G.; Zhang, K.; Shen, W.; Xu, G.; Lin, Y. Intelligent fault diagnosis of multi-way directional valves in hydraulic systems using digital twin and deep learning approaches. *Mech. Syst. Signal Process.* **2025**, *230*, 112579. [CrossRef]
22. Chen, H.; Chen, Q.; Yang, X.; Wang, X.; Chen, H. Omni-directional attitude detection of advanced hydraulic support relative to roadway based on visual measurement principle. *Opt. Laser Technol.* **2024**, *179*, 111329. [CrossRef]
23. Liang, M.; Zheng, D.; Fang, X.; Li, K.; Gu, C.; Wu, G.; Chen, N.; Feng, H. Research on attitude monitoring and decision-making of hydraulic support based on FBG sensor and BP neural network. *Opt. Fiber Technol.* **2025**, *93*, 104219. [CrossRef]
24. Hao, Z.; Xie, J.; Wang, X.; Feng, Z.; Meng, H. A method for reconstructing the pose of hydraulic support group based on point cloud and digital twin. *Measurement* **2024**, *225*, 113977. [CrossRef]
25. Jiao, X.; Xie, J.; Wang, X.; Yan, Z.; Hao, Z.; Wang, X. Intelligent decision method for the position and attitude self-adjustment of hydraulic support groups driven by a digital twin system. *Measurement* **2022**, *202*, 111722. [CrossRef]
26. Chen, H.; Chen, Q.; Chen, H.; Yang, X.; Wang, X. Measurement of displacement and top beam attitude angle of advanced hydraulic support based on visual detection. *Measurement* **2023**, *219*, 113264. [CrossRef]
27. Li, S.; Xie, J.; Wang, X.; Mei, Z.; Cai, N. A digital twin-based bi-directional deduction method for the full-pose of the Floating connection mechanism. *Measurement* **2024**, *224*, 113905. [CrossRef]
28. Witek, M.; Prusek, S. Numerical calculations of shield support stress based on laboratory test results. *Comput. Geotech.* **2016**, *72*, 74–88. [CrossRef]
29. Wan, L.; Yu, X.; Zeng, X.; Ma, D.; Wang, J.; Meng, Z.; Zhang, H. Performance analysis of the new balance jack of anti-impact ground pressure hydraulic support. *Alex. Eng. J.* **2023**, *62*, 157–167. [CrossRef]
30. Hu, X.; Ji, X.; Liu, Y.; Du, Y. Study on instability mechanism of hydraulic support in downdip and updip coal face. *Alex. Eng. J.* **2023**, *81*, 304–318. [CrossRef]
31. Ren, H.; Zhang, D.; Gong, S.; Zhou, K.; Xi, C.; He, M.; Li, T. Dynamic impact experiment and response characteristics analysis for 1:2 reduced-scale model of hydraulic support. *Int. J. Min. Sci. Technol.* **2021**, *31*, 347–356. [CrossRef]

32. Yang, X.; Wang, R.; Wang, H.; Yang, Y. A novel method for measuring pose of hydraulic supports relative to inspection robot using LiDAR. *Measurement* **2020**, *154*, 107452. [CrossRef]
33. Liang, M.; Fang, X.; Li, S.; Wu, G.; Ma, M.; Zhang, Y. A fiber bragg grating tilt sensor for posture monitoring of hydraulic supports in coal mine working face. *Measurement* **2019**, *138*, 305–313. [CrossRef]
34. Luo, C.; Fan, X.; Ni, J.; Yang, H.; Zhang, X.; Li, W. Positioning accuracy evaluation for the collaborative automation of mining fleet with the support of memory cutting technology. *IEEE Access* **2016**, *4*, 5764–5775. [CrossRef]
35. Jasiulek, D.; Bartoszek, S.; Perutka, K.; Korshunov, A.; Jagoda, J.; Plonka, M. Shield support monitoring system—Operation during the support setting. *Acta Montan Slovaca* **2019**, *24*, 391–401.
36. Zhang, Y.; Zhang, H.; Gao, K.; Xu, W.; Zeng, Q. New method and experiment for detecting relative position and posture of the hydraulic support. *IEEE Access* **2019**, *7*, 181842–181854. [CrossRef]
37. Gao, K.; Xu, W.; Zhang, H.; Zhang, Y.; Zeng, Q.; Sun, L. Relative position and posture detection of hydraulic support based on particle swarm optimization. *IEEE Access* **2020**, *8*, 200789–200811. [CrossRef]
38. Ge, X.; Xie, J.; Wang, X.; Liu, Y.; Shi, H. A virtual adjustment method and experimental study of the support attitude of hydraulic support groups in propulsion state. *Measurement* **2020**, *158*, 107743. [CrossRef]
39. Chen, H.; Chen, H.; Xu, Y.; Zhang, D.; Ma, Y.; Mao, J. Research on attitude monitoring method of advanced hydraulic support based on multi-sensor fusion. *Measurement* **2022**, *187*, 110341. [CrossRef]
40. Tutak, M.; Brodny, J.; Galecki, G. Applying CFD model studies to determine zones at risk of methane explosion and spontaneous combustion of coal in goaves. *Acta Montan Slovaca* **2022**, *27*, 651–666.
41. Cai, N.; Xie, J.; Wang, X.; Liu, S.; Du, W. Method for the relative pose reconstruction of hydraulic supports driven by digital twins. *IEEE Sens. J.* **2023**, *23*, 4707–4719. [CrossRef]
42. Feng, Z.; Xie, J.; Yan, Z.; Mei, Z.; Zheng, Z.; Li, T. An information processing method of software and hardware coupling for VR monitoring of hydraulic support groups. *Multimed. Tools Appl.* **2023**, *82*, 19067–19089. [CrossRef]
43. Peng, S.S.; Hsiung, S.M.; Jiang, Y.M. Evaluation of shield support performance by numerical analysis. *Min. Sci. Technol.* **1988**, *7*, 19–30. [CrossRef]
44. Peng, S.; Cheng, Z.; Che, L.; Zheng, Y.; Cao, S. Kinematic performance analysis of a parallel mechanism for loading test of hydraulic support. *Mech. Mach. Theory* **2022**, *168*, 104592. [CrossRef]
45. Guo, W.; Wang, H.; Dong, G.; Li, L.; Huang, Y. A case study of effective support working resistance and roof support technology in thick seam fully-mechanized face mining with hard roof conditions. *Sustainability* **2017**, *9*, 935. [CrossRef]
46. Kang, H.; Gao, F.; Xu, G.; Ren, H. Mechanical behaviors of coal measures and ground control technologies for China's deep coal mines – A review. *J. Rock Mech. Geotech. Eng.* **2023**, *15*, 37–65. [CrossRef]
47. Meng, Z.; Zeng, Q.; Gao, K.; Kong, S.; Liu, P.; Wan, L. Failure analysis of super-large mining height powered support. *Eng. Fail. Anal.* **2018**, *92*, 378–391. [CrossRef]
48. Zhang, Q.; Shi, P.; Li, M.; Zong, T.; Song, W. A design method and application of backfilling hydraulic supports in reforming top-coal caving hydraulic supports. *Appl. Sci.* **2023**, *13*, 987. [CrossRef]
49. Meng, Z.; Zeng, Q.; Wan, L.; Liu, P. Pose adjusting simulation of hydraulic support based on mechanical-electrical-hydraulic coordination. *Teh. Vjesn. Tech. Gaz.* **2018**, *25*, 1110–1118.
50. Guan, E.; Miao, H.; Li, P.; Liu, J.; Zhao, Y. Dynamic model analysis of hydraulic support. *Adv. Mech. Eng.* **2019**, *11*, 1687814018820143. [CrossRef]
51. Yang, Z.; Sun, Z.; Jiang, S.; Mao, Q.; Liu, P.; Xu, C. Structural analysis on impact-mechanical properties of ultra-high hydraulic support. *Int. J. Simul. Model.* **2020**, *19*, 17–28. [CrossRef]
52. Singh, G.; Singh, U. A numerical modeling approach for assessment of progressive caving of strata and performance of hydraulic powered support in longwall workings. *Comput. Geotech.* **2009**, *36*, 1142–1156. [CrossRef]
53. Verma, A.; Deb, D. Numerical Analysis of an Interaction between Hydraulic-Powered Support and Surrounding Rock Strata. *Int. J. Geomech.* **2013**, *13*, 181–192. [CrossRef]
54. Ralston, J.C.; Reid, D.C.; Dunn, M.T.; Hainsworth, D.W. Longwall automation: Delivering enabling technology to achieve safer and more productive underground mining. *Int. J. Min. Sci. Technol.* **2015**, *25*, 865–876. [CrossRef]
55. Cao, L.; Sun, S.; Zhang, Y.; Guo, H.; Zhang, Z. The research on characteristics of hydraulic support advancing control system in coal mining face. *Wirel. Pers. Commun.* **2018**, *102*, 2667–2680. [CrossRef]
56. Cheng, J.; Wan, Z.; Ji, Y. Shield-roof interaction in longwall panels: Insights from field data and their application to ground control. *Adv. Civ. Eng.* **2018**, *2018*, 3031714. [CrossRef]
57. Zeng, X.; Meng, G.; Zhou, J. Analysis on the pose and dynamic response of hydraulic support under dual impact loads. *Int. J. Simul. Model.* **2018**, *17*, 69–80. [CrossRef] [PubMed]
58. Zeng, Q.; Li, Y.; Yang, Y. Dynamic analysis of hydraulic support with single clearance. *Fac. Mech. Eng.* **2021**, *67*, 53–66. [CrossRef]

59. Yang, Y.; Zhang, Y.; Zeng, Q.; Wan, L.; Zhang, Q. Simulation research on impact contact behavior between coal gangue particle and the hydraulic support: Contact response differences induced by the difference in impacted location and impact material. *Materials* **2022**, *15*, 3890. [CrossRef]
60. Yuan, X.; Xie, J.; Gao, F.; Lian, Z. Assessment of shield support performance based on an innovative mathematical-physical model in longwall faces. *Proc. Inst. Mech. Eng. Part C J. Mech. Eng. Sci.* **2022**, *236*, 8935–8954. [CrossRef]
61. Zhai, G.; Yang, X. Modelling and analysis of a hydraulic support prop under impact load. *J. South. Afr. Inst. Min. Metall.* **2022**, *122*, 397–405. [CrossRef]
62. Li, Y.; Zeng, Q.; Wan, L. Dynamics analysis and motion prediction of caving mechanism with clearance of hydraulic support. *Alex. Eng. J.* **2024**, *105*, 783–797. [CrossRef]
63. Guo, J.; Huang, W.; Feng, G.; Bai, J.; Li, L.; Wang, Z.; Yu, L.; Wen, X.; Zhang, J.; Feng, W. Stability analysis of longwall top-coal caving face in extra-thick coal seams based on an innovative numerical hydraulic support model. *Int. J. Min. Sci. Technol.* **2024**, *34*, 491–505. [CrossRef]
64. Zhou, Y. Study of two-leg shield supporting ability areas theroy. *J. Fuxin Minging Inst.* **1993**, *12*, 46–49.

Disclaimer/Publisher's Note: The statements, opinions and data contained in all publications are solely those of the individual author(s) and contributor(s) and not of MDPI and/or the editor(s). MDPI and/or the editor(s) disclaim responsibility for any injury to people or property resulting from any ideas, methods, instructions or products referred to in the content.